Influence of through-flow on linear pattern formation properties in binary mixture convection

Ch. Jung, M. Lücke, and P. Büchel
Institut für Theoretische Physik, Universität des Saarlandes, D-66041 Saarbrücken, Germany
(Received 16 April 1996)

We investigate how a horizontal plane Poiseuille shear flow changes linear convection properties in binary fluid layers heated from below. The full linear field equations are solved with a shooting method for realistic top and bottom boundary conditions. Relevant characteristic growth exponents and the spatial structure of their associated eigenfunctions are evaluated for different perturbations of the conductive state. Through-flow induced changes of the bifurcation thresholds (stability boundaries) for different types of convective solutions are determined in the control parameter space spanned by Rayleigh number, Soret coupling (positive as well as negative), and through-flow Reynolds number. We elucidate the through-flow induced lifting of the Hopf symmetry degeneracy of left and right traveling waves in mixtures with negative Soret coupling. Finally we determine with a saddle point analysis of the complex dispersion relation of the field equations over the complex wave number plane the borders between absolute and convective instabilities for different types of perturbations in comparison with the appropriate Ginzburg-Landau amplitude equation approximation. [S1063-651X(96)11208-3]

PACS number(s): 47.20.Bp, 47.15.−x, 47.54.+r, 47.60.+i

I. INTRODUCTION

An externally imposed flow can influence the spatiotemporal behavior of dissipative structures growing in forced nonequilibrium systems. Examples are chemical and reaction-diffusion systems, biological problems, and the large variety of different hydrodynamic instabilities leading to pattern formation [1]. Here we theoretically investigate with a linear analysis of the relevant field equations the spatiotemporal properties of convection solutions that bifurcate out of the homogeneous, conductive state in a binary fluid layer heated from below.

A lot of experimental [2–10], analytical [11–17], and numerical [18–21] activities have been devoted recently to investigating these primary convection patterns in the absence of through-flow [22]. They revealed a variety of bifurcation properties and spatiotemporal behavior that is much richer than that of stationary mirror symmetric roll patterns growing in the supercritical bifurcation of the standard Rayleigh-Bénard setup with a pure fluid, say water. In binary mixtures such as, e.g., ethanol-water there occur stationary square and roll patterns but also symmetry degenerate left or right traveling convection waves. The bifurcation of the traveling wave (TW) solutions and of the stationary roll patterns can be supercritical, tricritical, or subcritical relative to the critical heating rate. These different solution properties are controlled by the combination of thermal forcing — i.e., the Rayleigh number — and the strength ψ [1] of the Soret coupling between temperature and concentration field. It is the concentration field that causes the rich structure formation behavior via its contribution to the buoyancy force field which drives convection.

Without lateral through-flow several experimental and theoretical papers have addressed the linear convection properties [25–37]. The most comprehensive and most accurate results were obtained in the more recent numerical work [31–37]. In this work we determine how a lateral through-flow changes the structure and dynamics of convection fields at onset. We evaluate relevant characteristic exponents and the spatial structure of their associated eigenfunctions for different perturbations of the conductive basic state and determine the through-flow induced changes of the bifurcation thresholds for different types of convective solutions. These thresholds are defined by vanishing real parts of the characteristic exponents. They mark stability boundaries of the conductive state against different convective perturbations in the control parameter space spanned by the Rayleigh number Ra, the Soret coupling ψ, and the through-flow Reynolds number Re. We have numerically solved the full linear field equations subject to realistic boundary conditions using a shooting method for perturbations with wave vectors parallel to the through-flow. The solutions for other wave vectors can be obtained from the former by a straightforward symmetry transformation. Results were obtained for positive as well as for negative ψ. For $\psi<0$ the most important result is that the through-flow lifts the Hopf symmetry degeneracy of left and right traveling waves at $Re=0$: frequencies, bifurcation thresholds, and structural properties of the two waves are changed dramatically. Mixtures with more negative ψ require a larger Re for the changes to reach a comparable relative size. For sufficiently large Re the lowest relevant bifurcation threshold of binary mixtures with any ψ asymptotically approaches the critical Rayleigh number $Ra_c(Re,\psi=0)$ of a pure fluid with imposed through-flow. Then the externally imposed shear flow eliminates the Soret-induced coupling effects between the convective concentration field and the other fields by suppressing vertical convective transport of Soret driven concentration perturbations.

Our paper is organized as follows. In Sec. II we describe the system. In Sec. III we review the linearized equations for perturbations of the conductive state, their boundary conditions, the eigenvalue problem for the characteristic exponents, relevant symmetry properties, and the behavior for small through-flow rates. Section IV contains our results concerning bifurcation properties — stability thresholds, wave numbers, frequencies, and eigenfunctions — for nega-

tive and positive Soret coupling ψ as functions of the through-flow Reynolds number Re. In Sec. V we compare borderlines between absolute and convective instabilities obtained for different types of perturbations from the field equations with results from the Ginzburg-Landau amplitude equation. The last section gives a brief summary of our work. Appendix A contains details of our shooting method. There we also describe our procedure to find saddle points of the dispersion relation of the field equations in the complex wave number plane. Appendix B presents results obtained from a variational calculus.

II. SYSTEM

We consider a horizontal layer of height d of a binary fluid mixture in the homogeneous gravitational field $\mathbf{g}=-g\mathbf{e}_z$ that is directed downwards. A positive temperature difference ΔT is imposed between the lower and upper confining boundaries, e.g., via highly conducting plates in experiments. The associated Rayleigh number is

$$Ra=\frac{\alpha g d^3}{\kappa\nu}\Delta T, \tag{2.1}$$

where κ is the thermal diffusivity and ν the kinematic viscosity. The thermal expansion coefficient α and the solutal expansion coefficient β follow from a linear isobaric equation of state for the total mass density

$$\rho=\rho_0[1-\alpha(T-T_0)-\beta(C-C_0)] \tag{2.2}$$

for small deviations of the temperature T from its mean T_0 and small deviations of the solute's mass concentration C from its mean C_0.

An externally applied lateral pressure gradient drives a through-flow in the x direction. The resulting mean lateral flow velocity U determines the through-flow Reynolds number

$$Re=U\frac{d}{\nu}. \tag{2.3}$$

We investigate here the parameter regime $0\leqslant Re\leqslant 1$. With $d\approx 0.5$ cm, $\nu\approx 0.01$ cm^2/s (H_2O) the maximal averaged through-flow velocity is then $U\approx 0.02$ cm/s, i.e., 1.2 cm per minute.

A. Equations

To describe this system we use the balance equations for mass, momentum, heat, and concentration in the Oberbeck-Boussinesq approximation [23,39]

$$\boldsymbol{\nabla}\cdot\mathbf{u}=0, \tag{2.4a}$$

$$(\partial_t+\mathbf{u}\cdot\boldsymbol{\nabla})\mathbf{u}=\sigma\nabla^2\mathbf{u}-\boldsymbol{\nabla}p+\sigma(T-T_0+C-C_0)\mathbf{e}_z, \tag{2.4b}$$

$$(\partial_t+\mathbf{u}\cdot\boldsymbol{\nabla})T=\nabla^2 T, \tag{2.4c}$$

$$(\partial_t+\mathbf{u}\cdot\boldsymbol{\nabla})C=L\nabla^2(C-\psi T). \tag{2.4d}$$

Here $\mathbf{u}=u\mathbf{e}_x+v\mathbf{e}_y+w\mathbf{e}_z$ is the velocity field. We reduce lengths by d, times by d^2/κ, the effective pressure p by κ^2/d^2, temperatures by $\kappa\nu/(\alpha g d^3)$, and the concentration field by $\kappa\nu/(\beta g d^3)$. Then the two material parameters Prandtl number

$$\sigma=\frac{\nu}{\kappa} \tag{2.5}$$

and Lewis number

$$L=\frac{D}{\kappa} \tag{2.6}$$

appear with D being the concentration diffusion constant. Furthermore, there enters the separation ratio

$$\psi=-\frac{\beta}{\alpha}\frac{k_T}{T_0}, \tag{2.7}$$

which measures the strength of the linear Soret coupling between concentration and temperature field via the thermodiffusivity k_T.

B. Conductive state

For small Ra,Re a laterally homogeneous solution of (2.4) is stable that describes a conductive state without vertical convective flow. It is a combination of plane horizontal Poiseuille flow

$$\mathbf{u}_{\rm cond}=U(z)\mathbf{e}_x=\sigma\ Re\ P(z)\mathbf{e}_x, \tag{2.8a}$$

$$P(z)=6\,z(1-z) \tag{2.8b}$$

and a diffusive temperature field

$$T_{\rm cond}=T_0+Ra(\tfrac{1}{2}-z), \tag{2.9}$$

which enforces via the Soret effect a diffusive vertical concentration stratification

$$C_{\rm cond}=C_0+Ra\ \psi(\tfrac{1}{2}-z). \tag{2.10}$$

III. CONVECTIVE PERTURBATIONS

Here we briefly review the linearized equations for perturbations of the conductive state, their boundary conditions, the eigenvalue problem for the characteristic exponents, relevant symmetry properties, and the behavior for small through-flow rates.

A. Linearization around the conductive state

1. Equations

The basis for our linear analysis of convective perturbations of the conductive state described in Sec. II B are the linearized field equations

$$(\partial_t-\sigma\nabla^2)\nabla^2 w+(U\nabla^2-\partial_z^2 U)\partial_x w=\sigma(\partial_x^2+\partial_y^2)(\theta+c), \tag{3.1a}$$

$$(\partial_t-\nabla^2+U\partial_x)\theta=Ra\,w, \tag{3.1b}$$

$$(\partial_t - L\nabla^2 + U\partial_x)c = \psi\, Ra\, w - L\psi\nabla^2\theta \tag{3.1c}$$

for the deviations

$$\theta = T - T_{\rm cond}, \quad c = C - C_{\rm cond} \tag{3.2}$$

from the conductive state (2.9),(2.10). Here w is the vertical velocity field that vanishes in the conductive state. To derive (3.1a) we have applied twice the curl operator to Eq. (2.4b) using (2.4a). Note that the Poiseuille flow profile $U(z)$ of the conductive state enters into Eqs. (3.1) making them nonautonomous.

2. NSI boundary conditions

We consider the horizontal boundaries to be perfectly heat conducting and rigid with no slip and vanishing vertical concentration transport. These, so called, NSI (no-slip, impermeable) conditions impose

$$\theta = w = \partial_z w = \partial_z \zeta = 0 \quad \text{at } z = 0,1. \tag{3.3}$$

Here we have introduced the combined field

$$\zeta = c - \psi\theta. \tag{3.4}$$

Since the concentration current at the no-slip boundaries is purely diffusive the condition $\partial_z\zeta = 0$ ensures impermeability of the horizontal boundaries. Laterally we assume the system to be unbounded.

3. FS boundary conditions

As an illustrative special case let us consider for the moment free slip (FS) horizontal boundaries with a shear-free plug flow profile, $U_{\rm FS}(z) = U$. In this idealized situation the effect of through-flow in Eqs. (3.1) can be transformed away by a Galilei transformation to a system that comoves with the vertically constant plug flow velocity $U = \sigma\, Re$. Thus, the stability properties of the FS conductive state are not changed by the horizontal plug flow. The stationary and oscillatory marginal stability curves of the mixture remain the same, only the characteristic exponents acquire an additional imaginary part of size $ik_x U$. This holds for FS horizontal boundaries irrespective of whether they are permeable or impermeable to the concentration field c.

B. Eigenvalue problem

The general solution of the perturbation equations (3.1) can be written as a superposition of plane-wave perturbations with lateral wave vector

$$\mathbf{k} = k_x\mathbf{e}_x + k_y\mathbf{e}_y. \tag{3.5}$$

The plane-wave solution ansatz for the fields

$$\Phi = (w, \theta, \zeta) \tag{3.6}$$

reads

$$\Phi(\mathbf{r}, t) = \hat{\Phi}(z)e^{i(k_x x + k_y y)}e^{st} \tag{3.7}$$

with a complex characteristic exponent

$$s = {\rm Re}s + i\ {\rm Im}s = \gamma - i\omega \tag{3.8}$$

and complex z-dependent amplitude functions $\hat{\Phi} = (\hat{w}, \hat{\theta}, \hat{\zeta})$. Inserting the ansatz (3.7) into the field equations (3.1) yields the 3×3 linear eigenvalue problem

$$(\mathcal{L} + s\mathcal{M})\hat{\Phi}(z) = 0 \tag{3.9a}$$

for the eigenvalues s and eigenvectors $\hat{\Phi}$ with

$$\mathcal{L} = \mathcal{L}^{(0)} + i\sigma k_x Re\, \mathcal{L}^{(1)}, \tag{3.9b}$$

$$\mathcal{L}^{(0)} = \begin{pmatrix} -\sigma(\partial_z^2 - k^2)^2 & \sigma(1+\psi)k^2 & \sigma k^2 \\ -Ra & k^2 - \partial_z^2 & 0 \\ 0 & \psi(\partial_z^2 - k^2) & L(k^2 - \partial_z^2) \end{pmatrix}. \tag{3.9c}$$

Into

$$\mathcal{L}^{(1)} = \begin{pmatrix} P(\partial_z^2 - k^2) - \partial_z^2 P & 0 & 0 \\ 0 & P & 0 \\ 0 & 0 & P \end{pmatrix} \tag{3.9d}$$

enters the vertical profile $P(z)$ (2.8b) of the Poiseuille through-flow and its second derivative. Finally

$$\mathcal{M} = \begin{pmatrix} \partial_z^2 - k^2 & 0 & 0 \\ 0 & 1 & 0 \\ 0 & 0 & 1 \end{pmatrix}. \tag{3.9e}$$

In the absence of through-flow $\mathcal{L}$ reduces to $\mathcal{L}^{(0)}$.

Due to the boundary conditions the eigenvalue spectrum is discrete. We are interested in the three characteristic exponents $s_j (j = 1,2,3)$ whose growth rates γ_j are closest to zero and whose eigenfunctions $\hat{\Phi}_j(z)$ have no nodes other than at the horizontal boundaries $z = 0,1$.

C. Symmetries

The solution of (3.9), i.e., eigenvalue s and eigenfunction $\hat{\Phi}$ depend on the material parameters σ and L, the control parameters ψ, Ra, Re, and on the lateral wave vector $\mathbf{k}$. Note first of all that the dynamics of perturbations with wave vectors perpendicular to the through-flow are not changed by the latter, since for them the contribution from $\mathcal{L}^{(1)}$ vanishes when $k_x = 0$.

1. Squire transformation

Since $\mathbf{k}$ and Re enter into (3.9) only as k^2 and $k_x Re$ the dependence of the functions $f = s, \hat{\Phi}$ on $\mathbf{k}$, and Re is

$$f = f(k^2, k_x Re). \tag{3.10}$$

Using this behavior the Squire transformation [38]

$$f(k_x^2 + k_y^2, k_x Re) = f(\tilde{k}_x^2, \tilde{k}_x \widetilde{Re}), \tag{3.11a}$$

$$\tilde{k}_x^2 = k_x^2 + k_y^2, \quad \widetilde{Re} = \frac{k_x}{\tilde{k}_x} Re \tag{3.11b}$$

relates the functions f for a wave vector with arbitrary components k_x, k_y to the functions that have been determined for wave vectors $\tilde{\mathbf{k}}=\tilde{k}_x\mathbf{e}_x$ in the through-flow direction and Reynolds numbers $\widetilde{Re}$. Therefore, we shall consider in the remainder of this work only $k_y=0$ perturbations with wave vectors $\mathbf{k}=k_x\mathbf{e}_x$ that are parallel or antiparallel to the through-flow. For $Re=0$ the Squire relations (3.11) reflect the horizontal rotational symmetry of the system in the absence of through-flow.

2. Reverting the through-flow direction

Upon reverting the flow direction, i.e., under the operation $Re\to -Re$ the set $\{s_j,\hat{\Phi}_j\}$ of eigenvalues and eigenfunctions transforms into each other since the balance equations (2.4) are invariant under the parity operation $(x,u)\to -(x,u)$ with u being the velocity field in the x direction. The transformation behavior of $\{s_j,\hat{\Phi}_j\}$ follows explicitly from the fact that the linear operator $\mathcal{L}$ entering the eigenvalue equation (3.9) transforms as

$$\mathcal{L}(-q_x)=\mathcal{L}^*(q_x),\quad q_x=k_xRe \tag{3.12}$$

under $Re\to -Re$ with the asterisk denoting complex conjugation. Here we do not display the other arguments of $\mathcal{L}$ that remain unchanged. We use (3.12) in the complex conjugate of Eq. (3.9):

$$[\mathcal{L}(-q_x)+s^*(q_x)\mathcal{M}]\hat{\Phi}_j^*(q_x)=0. \tag{3.13}$$

Thus, if $s_j(q_x)$ with $\hat{\Phi}_j(q_x)$ are solutions of (3.9) so are

$$\tilde{s}_j(q_x)=s_j^*(-q_x)\quad \text{with}\quad \tilde{\hat{\Phi}}_j(q_x)=\hat{\Phi}_j^*(-q_x). \tag{3.14}$$

Now, the nondegeneracy of the eigenvalue problem implies that the two sets $\{\tilde{s}_j,\tilde{\hat{\Phi}}_j\}$ and $\{s_j,\hat{\Phi}_j\}$ are the same. We find that one eigenvalue, say $j=3$, does not change — $\tilde{s}_3=s_3$ and $\tilde{\hat{\Phi}}_3=\hat{\Phi}_3$ — so that according to (3.14),

$$\gamma_3(-q_x)=\gamma_3(q_x), \tag{3.15a}$$

$$-\omega_3(-q_x)=\omega_3(q_x), \tag{3.15b}$$

$$\hat{\Phi}_3^*(-q_x)=\hat{\Phi}_3(q_x). \tag{3.15c}$$

The other two eigenvalues and eigenfunctions are cross-related to each other — $\tilde{s}_1=s_2,\hat{\Phi}_1=\hat{\Phi}_2$, and $\tilde{s}_2=s_1,\tilde{\hat{\Phi}}_2=\hat{\Phi}_1$ — so that according to (3.14),

$$\gamma_1(-q_x)=\gamma_2(q_x), \tag{3.16a}$$

$$-\omega_1(-q_x)=\omega_2(q_x), \tag{3.16b}$$

$$\hat{\Phi}_1^*(-q_x)=\hat{\Phi}_2(q_x). \tag{3.16c}$$

For $Re=0$ the relations (3.15) and (3.16) reflect the facts that in the absence of through-flow (i) the solutions depend on k_x^2 only, (ii) one eigenvalue is real, say $\omega_3=0$, with real eigenfunction $\hat{\Phi}_3=\hat{\Phi}_3^*$ that describes nonoscillatory dynamics, and (iii) the other two are a complex conjugate pair — $\gamma_1=\gamma_2,\omega_1=-\omega_2$ with $\hat{\Phi}_1^*=\hat{\Phi}_2$ — which describes the growth and/or decay of symmetry degenerate left and right traveling waves. This symmetry is broken by the through-flow. If for $Re=0$ all three eigenvalues and eigenfunctions are real then they fulfill for finite Re relations such as (3.15).

Since (3.15) and (3.16) relate the solutions for negative k_x, or Re to those with positive k_x or Re it suffices to investigate the three eigenvalues s_j and eigenfunctions $\hat{\Phi}_j$ for positive k_x, or Re only.

D. Expansion for small Reynolds numbers

It is instructive to see how the $Re=0$ solutions $\{s_j,\hat{\Phi}_j\}$ of the eigenvalue problem (3.9) evolve upon switching on the through-flow. The qualitative behavior can be studied *analytically* for small Re via an expansion in the parameter

$$\eta=\sigma q_x=\sigma k_xRe, \tag{3.17}$$

which appears explicitly in the linear operator $\mathcal{L}$ (3.9b)

$$\mathcal{L}=\mathcal{L}^{(0)}+i\eta\mathcal{L}^{(1)}. \tag{3.18a}$$

So we expand

$$s_j=s_j^{(0)}+\eta s_j^{(1)}+O(\eta^2), \tag{3.18b}$$

$$\hat{\Phi}_j=\hat{\Phi}_j^{(0)}+\eta\hat{\Phi}_j^{(1)}+O(\eta^2). \tag{3.18c}$$

Inserting (3.18) into (3.9a) yields in order η the equation

$$(i\mathcal{L}^{(1)}+s_j^{(1)}\mathcal{M})\hat{\Phi}_j^{(0)}=-(\mathcal{L}^{(0)}+s_j^{(0)}\mathcal{M})\hat{\Phi}_j^{(1)}, \tag{3.19}$$

which is solvable under the condition

$$\langle\hat{\Phi}_j^{(0)\dagger}|(i\mathcal{L}^{(1)}+s_j^{(1)}\mathcal{M})\hat{\Phi}_j^{(0)}\rangle = \int_0^1 dz(\hat{\Phi}_j^{(0)\dagger})^*(i\mathcal{L}^{(1)}+s_j^{(1)}\mathcal{M})\hat{\Phi}_j^{(0)}=0. \tag{3.20}$$

Here $\hat{\Phi}_j^{(0)\dagger}$ is the solution of the adjoint equation

$$(\mathcal{L}^{(0)\dagger}+s_j^{(0)\dagger}\mathcal{M}^\dagger)\hat{\Phi}_j^{(0)\dagger}=0 \tag{3.21}$$

of the zeroth-order eigenvalue problem

$$(\mathcal{L}^{(0)}+s_j^{(0)}\mathcal{M})\hat{\Phi}_j^{(0)}=0 \tag{3.22}$$

for the eigenvalue $s_j^{(0)}$. Note that $s_j^{(0)\dagger}=s_j^{(0)*}$ is the complex conjugate of the original eigenvalue $s_j^{(0)}$. The Fredholm alternative (3.20) leads to the first-order correction for s_j:

$$s_j^{(1)}=-ip_j, \tag{3.23}$$

where

$$p_j=\frac{\langle\hat{\Phi}_j^{(0)\dagger}|\mathcal{L}^{(1)}\hat{\Phi}_j^{(0)}\rangle}{\langle\hat{\Phi}_j^{(0)\dagger}|\mathcal{M}\hat{\Phi}_j^{(0)}\rangle} \tag{3.24}$$

is determined by normalized ''matrix elements'' of through-flow perturbation ''operators'' containing the profile $P(z)$ between the zeroth-order eigenfunctions

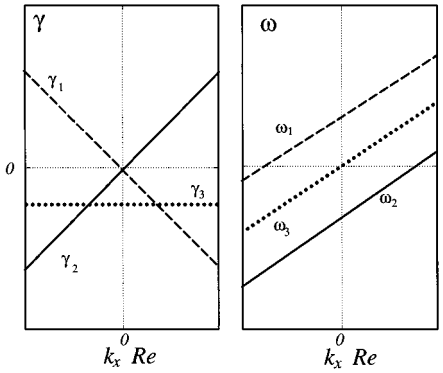

FIG. 1. Eigenvalues for small Reynolds numbers. The variation of growth rates γ and frequencies ω with Re resulting from an expansion up to linear order in Re is shown schematically. The lifting of the symmetry degeneracy, $s_2^{(0)}=s_1^{(0)*}$, by the through-flow and the behavior of $s_3^{(0)}$ is described in Sec. III D.

$\hat{\Phi}_j^{(0)}=(\hat{w}_j^{(0)},\hat{\theta}_j^{(0)},\hat{\zeta}_j^{(0)})$. Thus, the small-$Re$ expansion yields the following results for the eigenvalues $s_j=\gamma_j-i\omega_j$:

$$\gamma_j=\gamma_j^{(0)}+\eta\ \mathrm{Im}p_j+O(\eta^2), \tag{3.25a}$$

$$\omega_j=\omega_j^{(0)}+\eta\ \mathrm{Re}p_j+O(\eta^2). \tag{3.25b}$$

For the subsequent discussion we use the fact that the ''operators'' entering into the ''matrix elements'' of Eq. (3.24) are real.

1. Stationary perturbations

Let us call a perturbation stationary, for shorthand, if the characteristic exponent $s_j^{(0)}$ in the absence of through-flow is real. Then the corresponding eigenfunction is real as well, $\hat{\Phi}_j^{(0)}=\hat{\Phi}_j^{(0)*}$ which implies that also p_j (3.24) is real. Thus, with $\mathrm{Im}p_j=0$, one obtains from (3.25)

$$\gamma_j=\gamma_j^{(0)}+O(Re^2), \tag{3.26a}$$

$$\omega_j=\omega_j^{(0)}+\sigma k_x Re\,\mathrm{Re}p_j+O(Re^2). \tag{3.26b}$$

The frequency grows linearly with k_xRe while the growth rate is an even function of k_xRe for these stationary perturbations as shown schematically in Fig. 1 for the eigenvalue labeled by $j=3$.

2. Oscillatory perturbations

We call the perturbations oscillatory that are described by the two eigenvalues (say, $j=1,2$) that in the absence of through-flow form a complex conjugate pair, $s_2^{(0)}=s_1^{(0)*}$. The corresponding eigenfunctions are complex conjugates of each other, $\hat{\Phi}_2^{(0)}=\hat{\Phi}_1^{(0)*}$, according to (3.16), which implies $p_2=p_1^*$. With $\mathrm{Re}p_2=\mathrm{Re}p_1$ and $\mathrm{Im}p_2=-\mathrm{Im}p_1$ one obtains from (3.25) the following relations:

$$\gamma_{2}^{1}=\gamma_1^{(0)}\pm\sigma k_x Re\ \mathrm{Im}p_1+O(Re^2), \tag{3.27a}$$

$$\omega_{2}^{1}=\pm\omega_1^{(0)}+\sigma k_x Re\ \mathrm{Re}p_1+O(Re^2). \tag{3.27b}$$

Since with the plane-wave perturbation ansatz (3.7) the TW phase velocity ω/k_x should be increased for positive k_x and Re by the through-flow one can expect without having performed an explicit calculation that $\mathrm{Re}p_1$ in (3.27b) should be positive — cf. Fig. 1. And consequently both frequencies $\omega_{1,2}^{(0)}$ are shifted upwards by the same amount $\sigma k_x Re\,\mathrm{Re}p_1$. On the other hand, to decide whether the growth rate of the left or of the right traveling wave is increased or decreased requires an explicit calculation of $\mathrm{Im}p_1$. In any case, however, Eq. (3.27a) predicts that for small through-flow the symmetry degeneracy, $\gamma_1^{(0)}=\gamma_2^{(0)}$, of the growth rates is lifted by a symmetric splitting that increases linearly with Re as indicated schematically in Fig. 1 for γ_1 and γ_2.

For idealized FS boundary conditions the frequencies $\omega_j=\omega_j^{(0)}+\sigma k_x Re$ behave as in Fig. 1. However, the growth rates are independent of Re so that the degeneracy $\gamma_1^{(0)}=\gamma_2^{(0)}$ is not lifted by the FS plug flow.

IV. STABILITY AND BIFURCATION PROPERTIES

Here were present for negative as well as for positive Soret coupling ψ the Re dependence of critical properties: stability thresholds, wave numbers, frequencies, and eigenfunctions. These results have been obtained numerically by a variant [43] (cf. Appendix A 1 for a short description) of a standard shooting method that has previously been used [30] to determine stability properties of binary mixtures in the absence of through-flow [36]. In order to check these results — in particular some of the unexpectedly strong and peculiar changes with Re — by an independent method we have performed a variational calculation described in Appendix B.

A. Notation

We introduce Rayleigh numbers and wave numbers

$$r=\frac{Ra}{Ra_c(Re=0,\psi=0)}, \tag{4.1a}$$

$$\hat{k}=\frac{k}{k_c(Re=0,\psi=0)}, \tag{4.1b}$$

which are reduced by the critical ones of a pure fluid ($\psi=0$) in the absence of flow ($Re=0$)

$$Ra_c(Re=0,\psi=0)=1707.76, \tag{4.2a}$$

$$k_c(Re=0,\psi=0)=3.11632. \tag{4.2b}$$

As explained in Sec. III C, it suffices to consider wave vectors $\mathbf{k}=k_x\mathbf{e}_x$ in the through-flow direction with positive component $k_x=|\mathbf{k}|=k$. The spatiotemporal behavior of perturbations with other vectors follows with the symmetries of Sec. III C. We determine the evolution of the three relevant eigenvalues $s_j=\gamma_j-i\omega_j$ (cf. Sec. III B) upon increasing Re from $Re=0$ up to about 1. In particular we evaluate the critical parameter combinations for which each of the three growth rates γ_j first passes through zero when increasing r.

The so obtained critical quantities are marked by a subscript c and in addition by a superscript S, U, D that replaces the running index j of the three eigenvalues used in

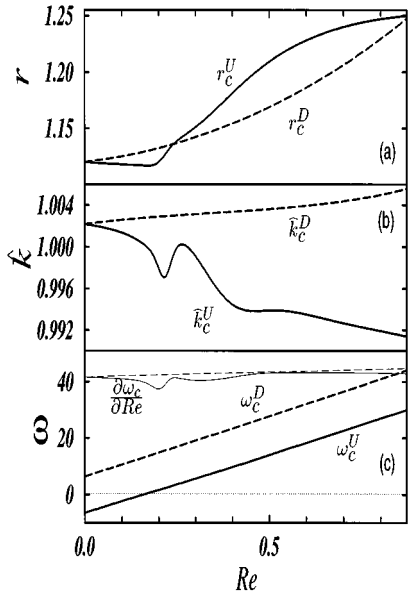

FIG. 2. Evolution of Hopf bifurcation properties with through-flow. Shown are critical Rayleigh numbers (a), reduced wave numbers (b), and frequencies (c) for upstream (full lines) and downstream (dashed lines) traveling perturbations that are symmetry degenerate for $Re=0$. Parameters are $L=0.01$, $\sigma=10$, $\psi=-0.1$.

Sec. III. The superscripts S, U, and D identify the critical perturbation behavior, $e^{i(k_c x-\omega_c t)}$, in the limit $Re\to 0$. Eigenvalues for which $\omega_c(Re\to 0)=0$ are marked by S since these perturbations are stationary for $Re=0$. Eigenvalues for which $\omega_c(Re\to 0)$ is positive (negative) carry the superscript D (U) since they characterize for $Re\to 0$ perturbations that propagate in the downstream (upstream) direction. We stress again that the cases S (''stationary''), D (''downstream''), and U (''upstream'') characterize the perturbations in the limit $Re\to 0$ — see also Fig. 1. In general all critical frequencies are finite in the presence of through-flow. However, for a special value of Re one has $\omega_c^U=0$ while ω_c^S and ω_c^D are positive (cf. Sec. IV B and Sec. IV C).

B. Effect of through-flow on the oscillatory instability

We present in this subsection critical properties of a binary mixture such as water-ethanol with $L=0.01$, $\sigma=10$, and separation ratio $\psi=-0.1$ as a representative case for a moderately negative Soret coupling. For these parameters the nonlinear solution of stationary convection in the absence of through-flow, $Re=0$, is already disconnected from the conductive state since the stationary bifurcation threshold r_c^S has moved already at $\psi_\infty^0=-L/(1+L)$ to infinity [27]. However, at $r_c^D=r_c^U=1.1200$ there is for $Re=0$ an oscillatory threshold into symmetry degenerated left and right — or in our language upstream and downstream — propagating traveling waves with critical wave numbers $\hat{k}_c^D=\hat{k}_c^U=1.0022$ and critical Hopf frequency $\omega_c^D=-\omega_c^U=6.4659$.

In Fig. 2 we show the variation of these two critical thresholds, wave numbers, and frequencies with increasing through-flow Reynolds numbers. In each case the full (dashed) line represents the upstream (downstream) critical quantity. Initially, for small Re, the bifurcation threshold $r_c^U(r_c^D)$ is depressed (enhanced) by the through-flow so that the conductive state is destabilized (stabilized) against convective perturbations traveling upstream (downstream) in comparison to the symmetry degenerate Hopf bifurcation threshold without through-flow — see also the schematic variation of the growth rates in Fig. 1. So at very small Re it is upstream traveling wave convection that grows first when increasing the Rayleigh number quasistatically.

However, while r_c^D increases monotonically with Re — first linearly and then quadratically — the initial linear downwards shift of r_c^U changes at larger Re to a precipitous increase and a subsequent flattening. Thus, in the shown Re range the two critical curves r_c^U and r_c^D have two intersections giving rise to bistable behavior of perturbations there. Note, however, that the bistable upstream and downstream TW perturbations cannot be superimposed linearly to a standing wave since their wave numbers $k_c^U\neq k_c^D$ differ and furthermore $\omega_c^U\neq-\omega_c^D$. So in the Re interval between the bistable intersections of r_c^U and r_c^D downstream propagating convection waves grow first while outside this interval at small Re and large Re upstream TW convection bifurcates first out of the conductive state.

Considering the critical wave numbers k_c^U and k_c^D of Fig. 2(b) it should be noted that their variation is very small — less than 2% — and that $k_c^U<k_c^D$ in the Re range of Fig. 2. This behavior holds also for the other Soret coupling strengths $\psi=-0.25,-0.01$, and -0.001 that we have investigated [43].

Somewhat unexpected to us is the nonmonotonical variation of k_c^U and also of $\partial\omega_c^U/\partial\, Re$ [Fig. 2(c)] in the interval below $Re=0.5$ where ω_c^U changes sign and where r_c^U shows its strong increase. To check that this variation is not a numerical artifact of our shooting algorithm we have performed a stability analysis with a variational approximation being a fundamentally different method. The variational results presented in Appendix B also show the peculiar variation of k_c^U with Re obtained from the shooting method thus supporting the latter behavior.

The critical frequencies ω_c^U and ω_c^D shown in Fig. 2(c) are practically linear functions of Re and in this respect similar to the frequencies of the idealized FS system. They start at zero through-flow with the Hopf values $|\omega_c^{(0)}|$ and $-|\omega_c^{(0)}|$, respectively, and they can be very well approximated by the first-order result (3.27b) of the low Re expansion

$$\omega_c=\omega_c^{(0)}+\sigma k_c^{(0)}\mathrm{Re}p_1 Re, \tag{4.3}$$

with $\sigma k_c^{(0)}\mathrm{Re}p_1\approx 41.9$ for $\sigma=10$. Comparing this rate of change $\partial\omega_c/\partial Re\approx 41.9$ with results for other separation ratios including the pure fluid case [42] one finds only very small deviations [43]. Obviously $\mathrm{Re}p_1$ (3.24) depends only weakly on the Soret coupling ψ.

Note that for $Re\geqslant|\omega_c^{(0)}|/41.9$ both critical frequencies, ω_c^D and ω_c^U, are positive. Then the phase velocities, $v_c=\omega_c/k_c$, of the two different critical TW's are in the positive x direction in the laboratory system, i.e., in through-flow direction. However, v_c^U is always smaller — by about $2|v_c^{(0)}|$ — than v_c^D. Only for $Re\leqslant|\omega_c^{(0)}|/41.9$ is the phase velocity v_c^U negative, i.e., opposite to the through-flow. So

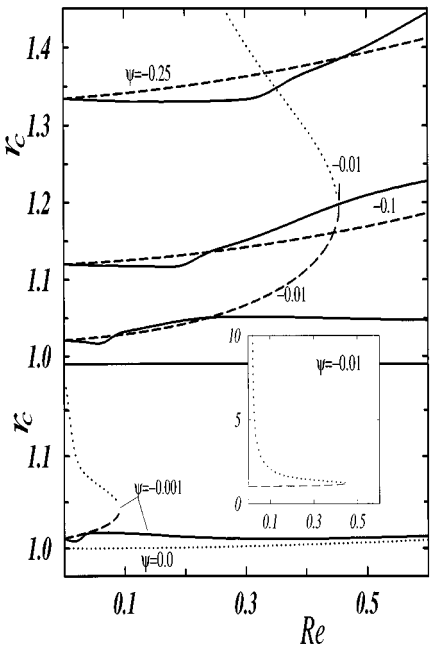

FIG. 3. Re dependence of bifurcation thresholds for negative Soret coupling ψ. The stability boundaries r_c^S (dotted lines), r_c^D (dashed lines), and r_c^U (full lines) are shown for some representative ψ values as indicated. The behavior beyond the Re values where r_c^D and r_c^S collide is discussed in Secs. IV C 4 and IV C 5. Parameters are $L=0.01$, $\sigma=10$.

the wording ''upstream propagating perturbations'' that we are using in this work does not necessarily imply that the phase velocity of such a TW is negative in the laboratory frame. It would be negative in a frame that is moving in the through-flow direction with a conveniently defined mean lateral velocity such as, e.g., $\overline{v}=\frac{1}{2}(v_c^D+v_c^U)$.

C. Bifurcation thresholds at negative ψ

In Fig. 3 we show the bifurcation thresholds r_c^U (full lines), r_c^D (dashed lines), and r_c^S (dotted lines) as functions of Re for a few characteristic negative Soret couplings ψ.

1. $r_c^U(Re,\psi)$

The typical shape of the stability curve r_c^U that is displayed in Fig. 2(a) for $\psi=-0.1$ does not change much for other negative separation ratios: As a function of Re r_c^U (full lines in Fig. 3) decreases for small Re, develops a minimum where ω_c^U goes through zero, steeply increases thereafter, and finally flattens asymptotically towards $r_c^S(Re,\psi=0)$ at large Re. Thus a sufficiently large through-flow eliminates the Soret induced coupling effects between concentration field on one side and temperature and velocity field on the other side: The bifurcation threshold $r_c^U(Re,\psi)$ approaches for any Soret coupling ψ the pure fluid stability boundary $r_c^S(Re,\psi=0)$ at large Re. For small ψ, e.g., at $\psi=-0.001$, the stability boundary r_c^U lies always below r_c^D while for larger $|\psi|$ (see, e.g., $\psi=-0.01$) there are two intersections of the curves r_c^D and r_c^U with $r_c^D \leqslant r_c^U$ in between — cf. the related discussion in Sec. IV B.

2. $r_c^D(Re,\psi)$

The bifurcation threshold r_c^D (dashed lines in Fig. 3) always increases monotonically with the through-flow strength. The initial slope $\partial r_c^D/\partial Re$ increases somewhat with decreasing $|\psi|$. For $\psi=-0.001$ and $\psi=-0.01$ the stability curves r_c^D and r_c^S collide in the Re range displayed in Fig. 3. This property is elucidated in Secs. IV C 4 and IV C 5 further below.

3. $r_c^S(Re,\psi)$

In pure fluids, $\psi=0$, the bifurcation threshold $r_c^S(Re,\psi=0)$ (lowest dotted curve in Fig. 3) slightly increases with growing Re [42]. In binary mixtures with negative Soret coupling, on the other hand, the stationary threshold r_c^S gets very strongly depressed by a small through-flow — see the dotted curve for $\psi=-0.001$ that starts at $r_c^S(Re=0,\ \psi=-0.001)=1.1816$.

In the absence of through-flow, $Re=0$, the threshold r_c^S rapidly increases with $|\psi|$ and diverges at $\psi_\infty^0=-L/(1+L)\simeq-0.0099$ for $L=0.01$. Beyond this Soret coupling the solution branch of stationary nonlinear convection is disconnected from the ground state solution as $r_c^S(Re=0,\ \psi\leqslant\psi_\infty^0)=\infty$. A small but finite through-flow, however, moves the threshold r_c^S down to finite values: The dotted curve for r_c^S in the inset of Fig. 3 for $\psi=-0.01<\psi_\infty^0$ shows (i) that $r_c^S=\infty$ below a finite $Re_\infty\approx0.019$, (ii) that r_c^S is finite for $Re>Re_\infty$, and (iii) that r_c^S steeply drops down for $Re>Re_\infty$. The Reynolds number Re_∞ where r_c^S diverges grows with increasing $|\psi|$ — a stronger Soret coupling requires a larger through-flow to move the bifurcation threshold r_c^S from infinity to a finite value.

4. Collision of the r_c^D and r_c^S stability boundaries

With increasing Re the bifurcation thresholds r_c^S and r_c^D approach each other. The former decreases rapidly and the latter increases with Re and they almost coalesce in the Re-r plane of Fig. 3. This behavior is most easily understood by investigating how the relevant eigenvalues $s=\gamma-i\omega$ vary with r and Re. To that end we show in Fig. 4 $\gamma(r)$ and $\omega(r)$ of the two relevant eigenvalues for a representative Soret coupling $\psi=-0.01$ at $Re=0$ (thick curves) and at $Re=0.4$ (thin curves) for a fixed wave number $\hat{k}=1$. The real part of the third eigenvalue is always negative in the parameter range of Fig. 4 and thus irrelevant for the following. Figure 5 shows in a *schematic* way the motion of these two eigenvalues in the complex s plane with increasing r for $Re=0$ (thick curves) and for a small $Re\neq0$ (thin curves).

Let us consider first $Re=0$. Then there is for small r a complex conjugate pair of eigenvalues ($\gamma^U=\gamma^D, \omega^U=-\omega^D$) that produce the symmetry degenerate Hopf bifurcation [at $r^D=r^U\approx1.021$ in Fig. 4(b)] when γ^U and γ^D pass simultaneously through zero. This situation is marked in Fig. 4 and Fig. 5 by thick upwards and downwards pointing triangles. With increasing r the real parts γ grow and the frequencies ω approach zero and the pair of eigenvalues meets in the complex s plane of Fig. 5 on the real γ axis (i.e., in Fig. 4 at $r\approx1.231$). Then, at larger r, this pair of real eigenvalues splits and moves apart along the real γ axis (cf. thickly dotted $S1$ and $S2$ curves in Figs. 4 and 5). So we

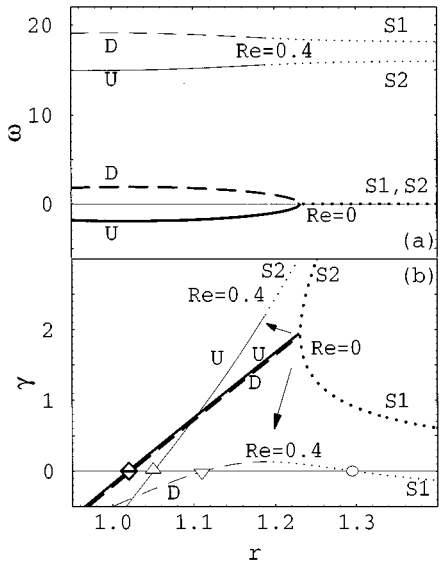

FIG. 4. (a) Frequencies $\omega(r)$ and (b) growth rates $\gamma(r)$ of the two eigenvalues that cause collision of the stability curves r_c^D and r_c^S in Fig. 3. Thick (thin) lines and symbols referring to $Re=0$ ($Re=0.4$) were obtained for a fixed wave number $\hat{k}=1$. Arrows indicate deformation directions of the curves. The Re variation of the zeros of γ at r^U (upwards pointing triangle), r^D (downwards pointing triangle), and r^S (circle) is discussed in Sec. IV C 4. Parameters are $L=0.01$, $\sigma=10$, $\psi=-0.01$.

have a transformation of two oscillatory eigenvalues (U and D) into two stationary ones ($S1$ and $S2$). For $Re=0$ the two thickly dotted branches γ^{S1} and γ^{S2} in Fig. 4(b) remain above zero, i.e., $S1$ does not reach the imaginary axis in Fig. 5.

Now for finite Re the symmetry degeneracy of the Hopf eigenvalue pair is lifted. The r value where γ^U goes through zero [upward pointing triangle at $r^U \approx 1.05$ in Fig. 4(b)] differs from the one where $\gamma^D=0$ [downward pointing triangle at $r^D \approx 1.112$ in Fig. 4(b)] and the frequencies ω^U and ω^D [thin lines in Fig. 4(a)] are shifted upwards. Thus the $Re=0$ pitchfork topology of the eigenvalue paths in Fig. 5 is

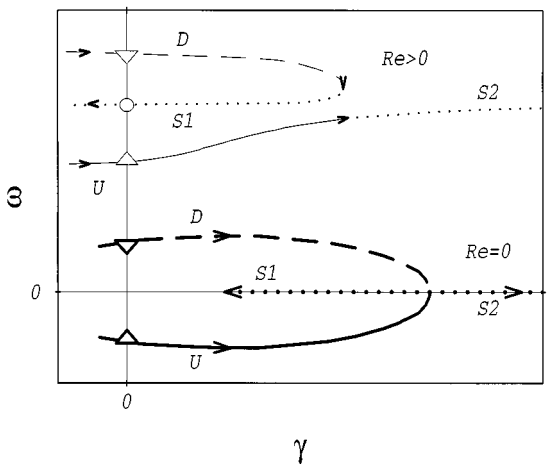

FIG. 5. *Schematic* variation of the eigenvalues of Fig. 4 in the complex γ-ω plane. Arrows indicate the motion of the eigenvalues with increasing r. Line styles and symbols are those of Fig. 4.

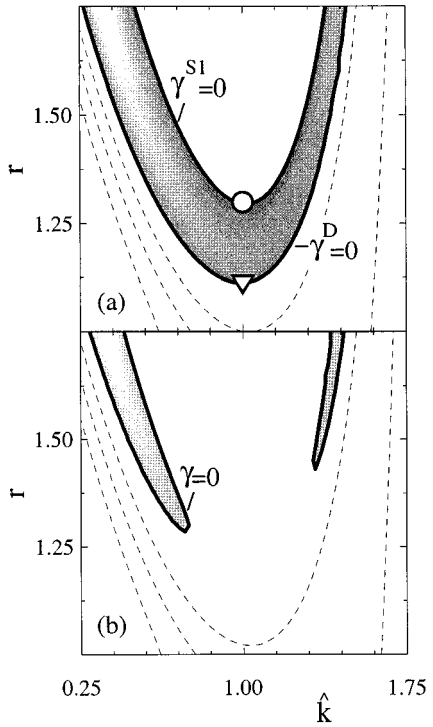

FIG. 6. The ''mountain landscape'' of $\gamma^{D/S}$ over the $\hat{k}$-r plane for $Re=0.4$ (a) and $Re=0.475$ (b). Gray scales show the height of $\gamma^{D/S}$ in the range where $\gamma>0$. Thick lines are marginal stability curves where $\gamma=0$. In the white parts of the figures is $\gamma^{D/S}<0$. Dashed lines are iso-γ lines. The zeros of $\gamma^{D/S}$ marked by circle and downwards pointing triangle are those of Fig. 4(b). Parameters are $L=0.01$, $\sigma=10$, and $\psi=-0.01$.

perturbed. Moreover, the eigenvalue branches become disconnected (thin lines in Fig. 5) as the thick eigenvalue branches of Fig. 4 are deformed by the through-flow into the thin ones — the arrows in Fig. 4(b) indicate the deformation directions. In particular the lower γ^{S1} branch of Fig. 4(b) and similarly the left moving $S1$ branch in Fig. 5 goes at a sufficiently large Re through zero at the circle in Figs. 4 and 5 thereby producing an S instability for $\hat{k}=1$ at the circle, i.e., at a finite value of r^S [≈ 1.296 in Fig. 4(b)]. Coming from ∞ the $S1$ intersection (circle) in Fig. 4(b) has moved with increasing Re to the left to finite value r^S. By increasing Re further the thin $D/S1$ curve in Fig. 4(b) is pushed downwards towards smaller γ, i.e., to the left in Fig. 5. Thereby the zero crossings at r^D (downward pointing triangle) and r^S (circle) move together and vanish simultaneously at a particular Re value. Thereafter there is only the zero crossing of γ^U at r^U (upward pointing triangle). This is in principle what happens when the r_c^D and r_c^S curves in Fig. 3 at $\psi=-0.001$ and -0.01 approach each other with increasing Re.

5. Opening of a wave number gap in the D-S marginal stability curves

The above described merging of the zeros of the $\gamma^{D/S1}$ curve that occurs in Fig. 4(b) for $\hat{k}=1$ slightly above $Re=0.4$ corresponds to the opening up of a gap in the marginal stability curves against D and S perturbations. This scenario is documented in the $\hat{k}$-r plane of Fig. 6. There we

show with gray scales the height distribution of $\gamma^{D/S1}$ in the $\hat{k}$-r range where $\gamma>0$. Thick lines labeled by $\gamma=0$ are marginal stability curves. In the white parts of Fig. 6 $\gamma^{D/S1}$ is negative and the dashed lines indicate γ isolines for $\gamma<0$. The third eigenvalue $\gamma^{U/S2}$ being positive — cf. Figs. 4 and 5 — is not shown. The open triangle and the circle in Fig. 6(a) mark the zeros of $\gamma^{D/S1}$ at $Re=0.4$, which are shown in Fig. 4(b) by the same symbols.

Upon increasing Re the eigenvalue $\gamma^{D/S1}$ decreases. Thus, the ''mountain landscape'' of $\gamma^{D/S1}$ somewhat globally ''sinks'' down. Thereby the $\gamma=0$ isolines come together in the $\hat{k}$-r plane of Fig. 6 and since the ''mountain ridge'' of $\gamma^{D/S1}$ does not have constant height [cf. gray scales in Fig. 6(a)] the $\gamma=0$ curves are connected into two tongues [Fig. 6(b)] that are separated by a wave number gap in which $\gamma^{D/S1}$ is negative. Increasing Re further the gap widens and the $\hat{k}$-r regions with $\gamma>0$ between the $\gamma=0$ isolines narrow down as the latter move away from $\hat{k}=1$ towards larger r.

We have difficulties resolving this behavior of the $\gamma=0$ isolines with our shooting method. We therefore show in Fig. 3 and later in Figs. 8 and 15 the minima r_c^D and r_c^S of the marginal stability curves only *before* the wave number gap opens. The ending of r_c^D and r_c^S in Figs. 3, 8, and 15 should therefore not be interpreted as a termination of bifurcation branches: after the opening up of the gap the tongue shaped stability curves move towards larger r and with them their minima.

D. Bifurcation properties at positive ψ

In the absence of through-flow there is only a stationary bifurcation threshold $r_c^S(Re=0,\psi)$ at $\psi\geqslant 0$ that strongly drops from $r_c^S(Re=0,\psi=0)=1$ towards zero when increasing ψ. Switching on the through-flow has the overall effect of increasing r_c^S towards $r_c^S(Re,\psi=0)$ as can be read off from Fig. 7. Thus the lateral flow stabilizes the basic state by eliminating in the so-called Soret regime [9] the convectively induced concentration homogenization. Note that already a very small through-flow has a dramatic stabilization effect: r_c^S increases very strongly for small Re. Similarly the critical wave number $\hat{k}_c^S$ [Fig. 7(b)] approaches with increasing Re the pure-fluid value $\hat{k}_c^S(Re,\psi=0)$.

E. Bifurcation surfaces in r-Re-ψ space

To give an impression of the form of the three critical surfaces in the r-Re-ψ space where U, D, and S convection patterns bifurcate out of the conductive state we combine in Fig. 8 in a three-dimensional plot the Re dependence of the bifurcation thresholds r_c^U (thin full lines), r_c^D (thin dashed lines), and r_c^S (thin dotted lines) presented so far together with their ψ dependence for $Re=0$ (thick lines). The bifurcation surfaces $r_c^D(Re,\psi)$ and $r_c^U(Re,\psi)$ emanate for negative Soret coupling $\psi<0$ out of the degenerate Hopf threshold line $r_c^D(Re=0,\psi)=r_c^U(Re=0,\psi)$ (thick dashed and full line) and split apart when the through-flow is switched on. Upon increasing Re further r_c^U gets indented slightly. On the other hand, r_c^D curls up and comes very close to the surface

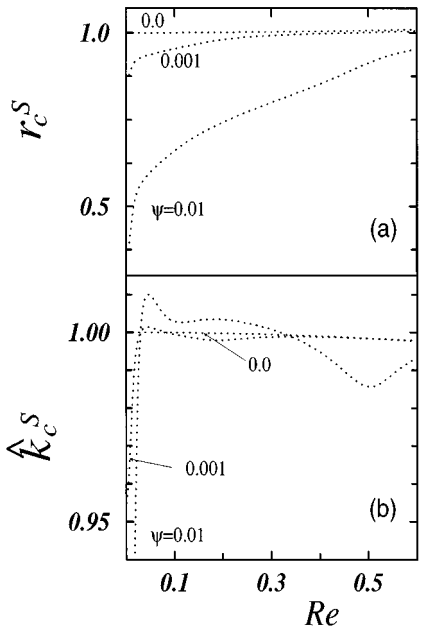

FIG. 7. (a) Critical Rayleigh numbers and (b) wave numbers for positive ψ versus through-flow Reynolds numbers. Parameters are $L=0.01$, $\sigma=10$.

$r_c^S(Re,\psi)$ which is strongly bent down by the through-flow for $\psi<0$. See Secs. IV C 4 and IV C 5 for a discussion of the further fate of these bifurcation surfaces.

The physically relevant, i.e., lowest lying, surface at larger Re is $r_c^U(Re,\psi)$ (thin full lines). For any $\psi<0$ it asymptotically approaches with increasing through-flow the $\psi=0$ stability threshold, i.e., $r_c^U(Re,\psi)\rightarrow r_c^S(Re,\psi=0)$. Thus a sufficiently large through-flow effectively eliminates the influence of any Soret coupling between *convective* concentration field and temperature and velocity fields (the dif-

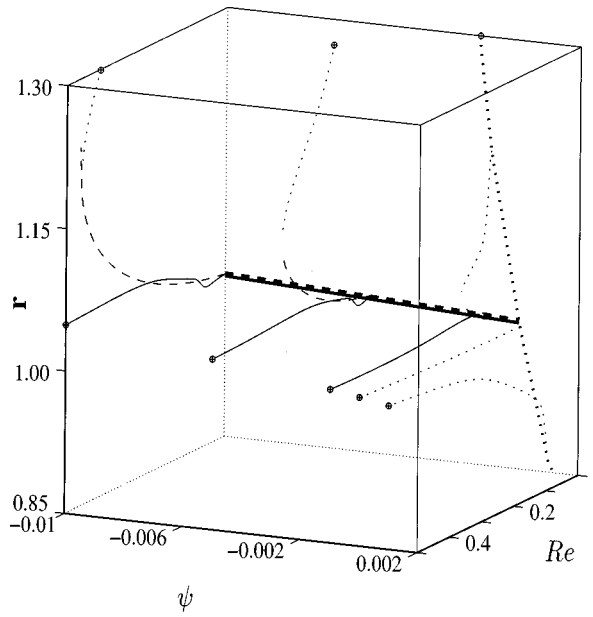

FIG. 8. To give an impression of the bifurcation surfaces in r-Re-ψ space we show r_c^U (thin full lines), r_c^D (thin dashed lines), and r_c^S (thin dotted lines) together with their ψ dependence for $Re=0$ (thick lines). Parameters are $L=0.01$, $\sigma=10$.

fusively induced concentration stratification in the conductive state (2.10), on the other hand, is not altered by the lateral shear flow). The bifurcation thresholds of the mixture approach that, $r_c^S(Re,\psi=0)$, of the pure fluid. This also holds for mixtures with positive Soret coupling — cf. the thin dotted line for $r_c^S(Re,\psi)$ at $\psi>0$.

F. Structure of critical convective patterns

Here we show how the spatial structure of the critical field deviations from the conductive state changes with increasing Re. To that end we have evaluated the complex eigenfunctions $\Phi(x,z,t)=\hat{\Phi}(z)e^{i(k_c x-\omega_c t)}$ at the critical thresholds r_c^D, r_c^U, and r_c^S. Thus the critical convective fields w,θ,c have the form

$$w(x,z,t)=|\hat{w}(z)|\cos[k_c x-\omega_c t-\varphi_w(z)] \tag{4.4}$$

and similarly for θ and c. Being solutions of complex linear equations we choose the abitrary complex scaling constant by fixing the modulus of the convective temperature field in the middle of the layer,

$$|\hat{\theta}(z=\tfrac{1}{2})|=1, \tag{4.5}$$

and by fixing the vertical mean of the phase $\varphi_w(z)$ of the vertical velocity field to zero

$$\int_0^1 dz\,\varphi_w(z)=0. \tag{4.6}$$

We present gray-scale contour plots of the fields w,θ, and c in the vertical x-z cross section of the fluid layer with white (black) denoting large (small) values. Each of Figs. 9, 11, 13 has nine contour lines denoting the fractions $\pm n/5$ of the maximal field values with $n=0,1,2,3,4$. In addition we present in Figs. 10, 12, 14 vertical profiles of the moduli and phases of the complex field amplitudes $\hat{w},\hat{\theta}$, and $\hat{c}$.

1. Propagating patterns for $Re=0$

First we briefly recall the critical TW field structure (top part of Fig. 9) in the absence of through-flow [30–32] for a relatively large Soret coupling $\psi=-0.25$. The TWs of velocity, temperature, and concentration are vertically not plane but their phases show a vertical variation that is largest for the concentration wave (Figs. 9 and 10). The lateral location of a concentration surplus (white ellipse in the c field of Fig. 9) phase lags by about a quarter wavelength behind the lateral position of vertical downflow (black ellipse in the w field). Thus, since the w field advectively transports concentration surplus (deficiency) from the Soret induced alcohol rich top (poor bottom) boundary layer into the bulk fluid this feeding mechanism between boundary layer and bulk is laterally phase shifted by roughly $\lambda/4$ in the propagating wave. Also the crest (valley) position of the temperature wave phase lags — albeit by a smaller amount — behind the lateral location of maximal vertical upwards (downwards) flow, which advectively feeds the bulk with warm (cold) fluid from the warm bottom (cold top) region. This phase lag agrees quite well with the result

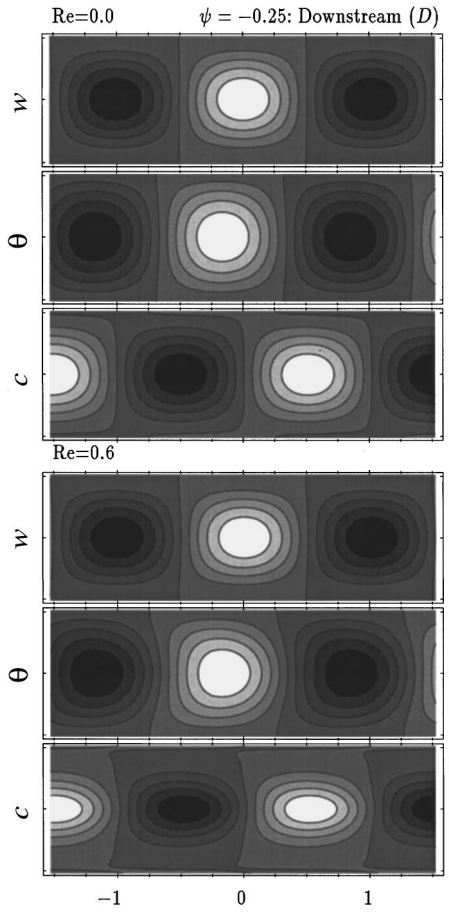

FIG. 9. Spatial structure of D patterns that propagate downstream, i.e., to the right. Contours of the fields w, θ, c in vertical cross sections of the fluid layer are shown for different Re as indicated. White (black) implies large (small) field values. The largest vertical up (down) flow is at $x=0(\pm 1)$. Contour lines mark fractions $\pm(0,1,2,3,4)/5$ of the field maxima. Parameters are $L=0.01$, $\sigma=10$, $\psi=-0.25$. The critical frequencies are about $\omega_c^D\approx 11.21+41.9Re$.

$$\varphi_w-\varphi_\theta\approx \arctan\left[\frac{\omega_c^{(0)}}{\pi^2+(k_c^{(0)})^2}\right] \tag{4.7}$$

obtained [16] from a Galerkin model.

As a result of the smallness of the Lewis number L, i.e., of the diffusive concentration transport the c field shows characteristic boundary layer behavior near the plates where advection decreases to zero — see the variation of the modulus $|\hat{c}(z)|$ and of the phase $\varphi_c(z)$ in Fig. 10. Whithin the boundary layers $|\hat{c}(z)|$ is suppressed and the phase lag of the c wave behind the w wave is significantly enlarged.

2. "Downstream" patterns

Upon turning on the through-flow the phase lines of the downstream propagating patterns get bent further (cf. Fig. 9 and in particular the right column of Fig. 10) and the phase differences between the different waves increase near the plates. The vertical moduli profiles of w and θ do not change. On the other hand, $|\hat{c}(z)|$ decreases (increases) near the plates (in the center of the fluid layer) so that the vertical profile of $|\hat{c}|$ flattens near the plates and becomes more

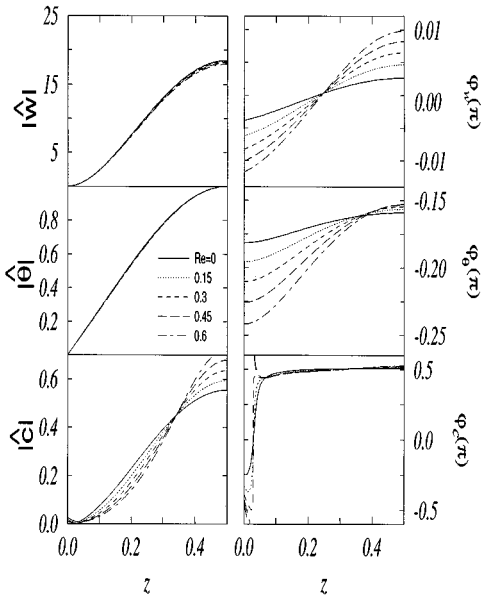

FIG. 10. Vertical profiles of D patterns. Shown are moduli (left column) and phases (right column) of the critical complex amplitudes that are symmetric around the mid position $z=1/2$. Their normalization is explained in Sec. IV F. Parameters are $L=0.01$, $\sigma=10$, $\psi=-0.25$.

peaked in the bulk near $z=1/2$. The phase lag of $\varphi_c(z)$ increases in the boundary layers with the through-flow.

The above described flow-induced structural changes of $\hat{c}(z)$ can easily be understood within the $L=0$ approximation [30,32] to the concentration field balance (3.1c)

$$\hat{c}(z)\approx i\psi Ra_c^D\frac{\hat{w}(z)}{\omega_c^D-\sigma k_c^D P(z)Re} \tag{4.8}$$

in a critical TW that is propagating downstream with the critical frequency ω_c^D. Thus for $L=0$, i.e. in the absence of diffusive concentration currents — which, by the way, is quite a good approximation to the real situation of ethanol-water mixtures with $L=0.01$ — the $\hat{c}(z)$ profile is advectively slaved to the vertical velocity $\hat{w}(z)$ and the through-flow velocity $U(z)=\sigma P(z)Re$: The prefactor i in (4.8) reflects the overall phase shift of $\pi/2$ between $\hat{w}$ and $\hat{c}$. The *effective z dependent* lateral velocity

$$u_{\rm eff}^D(z)=v_c^D-\sigma P(z)Re \tag{4.9}$$

that enters in the denominator of (4.8) renormalizes the profile $\hat{w}$ in the numerator of (4.8) so that the $L=0$ concentration profile

$$\hat{c}(z)\approx i\psi\frac{Ra_c^D}{k_c^D}\frac{\hat{w}(z)}{u_{\rm eff}^D(z)} \tag{4.10}$$

is determined by the quotient of these two velocity profiles. Since the phase velocity of the D wave, $v_c^D=\omega_c^D/k_c^D$, can well be approximated by

$$v_c^D\approx v_c^{(0)}+\sigma{\rm Re}p_1Re \tag{4.11}$$

according to (4.3) with ${\rm Re}p_1\approx 1.34$ we can rewrite the lateral velocity that is effective for the concentration distribution profile (4.10) of the D wave as

$$u_{\rm eff}^D(z)\approx v_c^{(0)}+\sigma Re[1.34-6\,z(1-z)]. \tag{4.12}$$

Thus, in the bulk $u_{\rm eff}^D(z=1/2)\approx v_c^{(0)}-0.16\sigma Re$ decreases with increasing through-flow while $u_{\rm eff}^D$ increases near the plates with Re, e.g., $u_{\rm eff}^D(z=1/4)\approx v_c^{(0)}+0.21\sigma Re$. This explains the flow-induced changes in the profile $\hat{c}$ (4.10) to be seen in Fig. 10 for $\psi=-0.25$ with $v_c^{(0)}=3.6$.

3. "Upstream" patterns

In the absence of through-flow the field structure of TWs propagating to the left, i.e., in the upstream direction is the mirror image of the $Re=0$ downstream patterns shown in the top part of Fig. 9. Therefore we have not included the $Re=0$ reference upstream pattern in Fig. 11 where we show upstream patterns for $Re=0.3$, 0.45, and 0.6.

Switching on the through-flow decreases and eventually reverts the original $Re=0$ phase bending of the w and θ waves (cf. right column in Fig. 12) while the moduli $|\hat{w}|$ and $|\hat{\theta}|$ remain practically unaffected by the through-flow of Figs. 11 and 12. On the other hand, the upstream concentration wave is significantly changed with increasing Re: $|\hat{c}(z)|$ develops two side maxima in the upper and lower half of the fluid layer while flattening in the center part (cf. left column of Fig. 12 or also Fig. 11). These structural changes of the c wave always occur in the Re range beyond the zero crossing of ω_c^U where also r_c^U and k_c^U show a significant variation. Thus, we infer that these phenomena are related to each other.

The flow-induced structural change of $\hat{c}(z)$ can be understood within the $L=0$ approximation

$$\hat{c}(z)\approx i\psi\frac{Ra_c^U}{k_c^U}\frac{\hat{w}(z)}{u_{\rm eff}^U(z)} \tag{4.13}$$

to the concentration balance (3.1c) in an upstream TW with effective lateral velocity

$$u_{\rm eff}^U(z)=v_c^U-\sigma P(z)Re. \tag{4.14}$$

Again $v_c^D=\omega_c^D/k_c^D$ can well be approximated by

$$v_c^U\approx -|v_c^{(0)}|+\sigma{\rm Re}p_1Re \tag{4.15}$$

so that

$$u_{\rm eff}^U(z)\approx -|v_c^{(0)}|+\sigma Re[1.34-6\,z(1-z)]. \tag{4.16}$$

Note, however, that ignoring the dissipative contribution $-L\nabla^2 c$ on the left-hand side of the concentration balance (3.1c) causes in the $L=0$ concentration profile [(4.13)–(4.16)] a divergence at

$$z_\pm=\frac{1}{2}\pm\frac{1}{2}\sqrt{1-\frac{2}{3}\left(1.34-\frac{|v_c^{(0)}|}{\sigma Re}\right)} \tag{4.17a}$$

via the zeros of $u_{\rm eff}^U(z)$ whenever

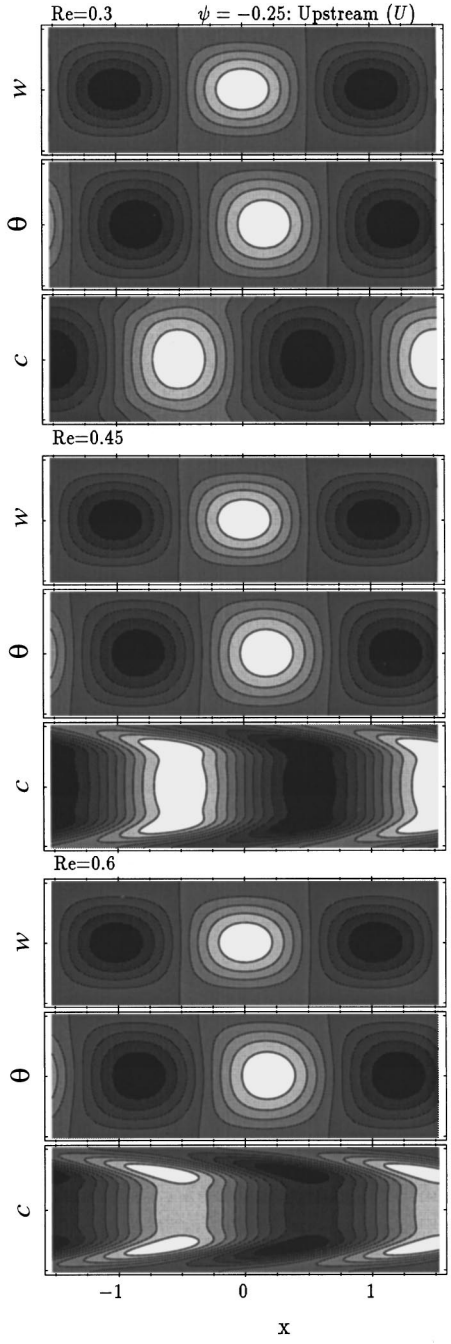

FIG. 11. Spatial structure of U patterns. They propagate for $Re \to 0$ upstream, i.e., to the left. Contours of the fields w, θ, c in vertical cross sections of the fluid layer are shown for different Re as indicated. White (black) implies large (small) field values. The largest vertical up (down) flow is at $x=0(\pm 1)$. Contour lines mark fractions $\pm(0,1,2,3,4)/5$ of the field maxima. Parameters are $L=0.01$, $\sigma=10$, $\psi=-0.25$. The critical frequencies are about $\omega_c^U \approx -11.21+41.9Re$.

$$Re > \frac{|v_c^{(0)}|}{1.34\sigma}. \tag{4.17b}$$

The diffusive contribution in (3.1c) prevents the divergence at $z_\pm$ leading to side maxima in $|\hat{c}(z)|$ instead (cf. Fig. 12 for $Re=0.45$ and 0.6). Their location is shifted slightly towards the bulk in comparison with, e.g., $z_-(Re=0.45)=0.1$ and $z_-(Re=0.6)=0.144$.

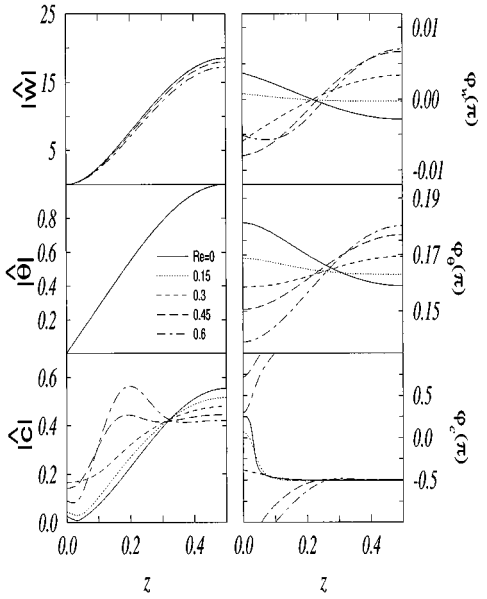

FIG. 12. Vertical profiles of U patterns. Shown are moduli (left column) and phases (right column) of the critical complex amplitudes that are symmetric around the mid position $z=1/2$. Their normalization is explained in Sec. IV F. Parameters are $L=0.01$, $\sigma=10$, $\psi=-0.25$.

It should be noted that for the large Soret coupling $\psi=-0.25$ the upstream fields displayed in Figs. 11 and 12 for $Re=0.6$ have not yet reached their asymptotic large-Re form — cf. also the bifurcation thresholds r_c^U in Fig. 3. For large Re the modulus $|\hat{c}(z)|$ decreases substantially and becomes more flat, as was observed [43] explicitly for smaller Soret coupling $\psi=-0.001,-0.01$.

4. "Stationary" patterns

Here we discuss the effect of through-flow on stationary patterns at a moderately positive Soret coupling, $\psi=0.01$, as a representative example. In the absence of through-flow, $Re=0$, the perturbation fields (top part of Fig. 13 and full lines of Fig. 14) are real, in phase, and laterally mirror symmetric around the vertical lines of maximal upflow ($x=0$) and downflow ($x=\pm 1$). Thus, for $Re=0$ the lateral locations of largest alcohol surplus (deficiency) coincide with the largest vertical upflow (downflow) velocity that feeds the bulk with warm, alcohol rich (cold, alcohol poor) fluid from the bottom (top) plate. Note that for $\psi>0$ the Soret effect causes concentration surplus (deficiency) at the warm (cold) plate. The critical convective concentration amplitude $|\hat{c}(z)|$ is for $Re=0$ so large that the full line representing it in Fig. 14 lies outside the chosen plot range. The critical wavelength $\lambda_c^{(0)}(\psi=0.01)=2.9833$ of the $Re=0$ pattern (top part in Fig. 13) is substantially larger than 2.

Already a small through-flow changes the above described field structure of stationary convective perturbations dramatically. The wavelength decreases toward 2. The flow amplitudes $|\hat{w}(z)|$ and even more conspicuously the concentration amplitude $|\hat{c}(z)|$ decrease. The phase $\varphi_c(z)$ of the concentration field exhibits a strong vertical variation reflecting the almost passive advection by the flow that is roughly characterized by the parabolic lateral through-flow profile su-

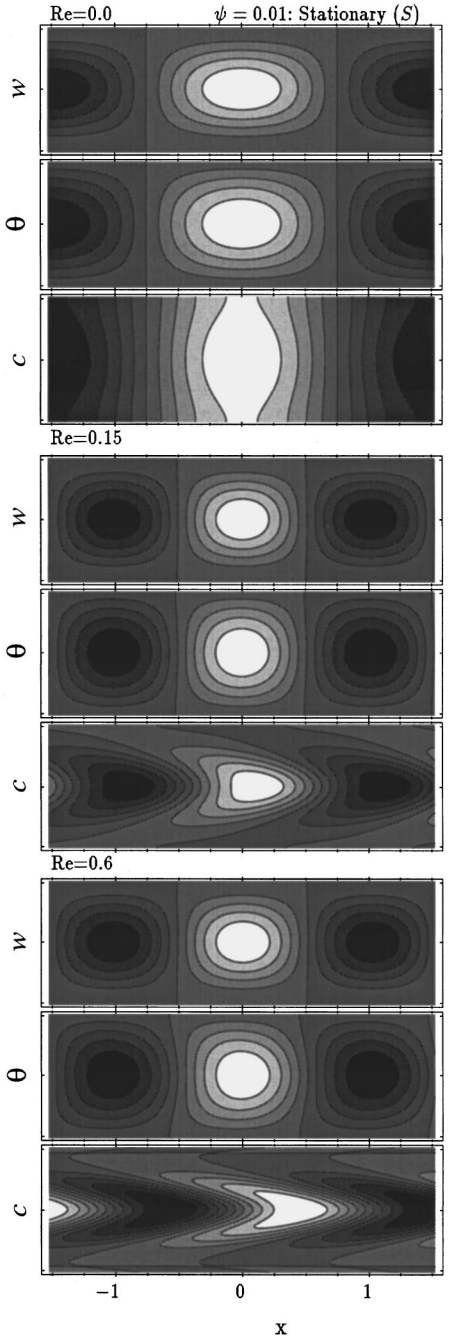

FIG. 13. Spatial structure of S patterns. They are stationary for $Re \to 0$. Contours of the fields w, θ, c in the vertical cross sections of the fluid layer are shown for different Re as indicated. White (black) implies large (small) field values. The largest vertical up (down) flow is at $x=0(\pm 1)$. Contour lines mark fractions $\pm(0,1,2,3,4)/5$ of the field maxima. Parameters are $L=0.01$, $\sigma=10$, $\psi=0.01$. The critical frequencies are about $\omega_c^S \approx 41.9Re$.

perimposed upon a roll-like closed-flow pattern.

For $\psi<0$, however, amplitudes and phases of S patterns become more and more similar to those of D patterns when the two bifurcation branches r_c^S and r_c^D approach each other with increasing Re in Fig. 8. However, the *critical* wave numbers of these two structures differ: For $\psi=-0.001$ we find $\hat{k}_c^D=1.001$ and $\hat{k}_c^S=0.998$ and for $\psi=-0.01$ the difference of the critical wave numbers

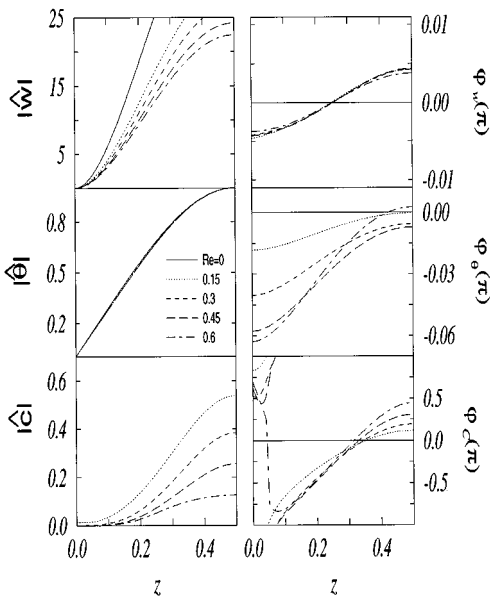

FIG. 14. Vertical profiles of S patterns. Shown are moduli (left column) and phases (right column) of the critical complex amplitudes that are symmetric around the mid position $z=1/2$. Their normalization is explained in Sec. IV F. Parameters are $L=0.01$, $\sigma=10$, $\psi=0.01$.

$(\hat{k}_c^D=1.089,\ \hat{k}_c^S=0.9678)$ increases. Thus, $\hat{k}_c^D-\hat{k}_c^S$ increases with $|\psi|$ when the bifurcation branches collide as described in Secs. IV C 4 and IV C 5.

V. ABSOLUTE AND CONVECTIVE INSTABILITY

Whenever at a stability threshold the frequency is nonzero with a finite group velocity

$$v_g=\left.\frac{\partial\omega(k)}{\partial k}\right|_{k_c} \tag{5.1}$$

one has to distinguish between spatiotemporal growth behavior of spatially extended and of spatially localized perturbations. The former having a form $\sim e^{ikx}$ have a positive growth rate above the bifurcation thresholds r_c determined in the previous section.

A. Wave packets, front propagation, and saddle point analysis

A spatially localized perturbation, i.e., a wave packet superposition of plane-wave extended perturbations of a particular kind moves in the so called convectively unstable parameter regime [44–47] with the velocity v_g faster away than it grows — while growing in the frame comoving with v_g the packet moves out of the system so that the basic conductive state is restored. In other words, the two fronts that join the wave packet's intensity envelope to the structureless state both propagate in the direction in which the packet center moves. On the other hand, in the so called absolutely unstable parameter regime the growth rate of the packet is so large that one front propagates opposite to the center motion. Thus the packet expands in the laboratory frame into the direction of packet motion as well as opposite to it [44,45].

We would like to emphasize that we are dealing here only with a linear analysis of the convective fields. Thus we do not address the question whether, e.g., at a subcritical bifurcation the above decribed wave packet grows to a stable nonlinear state that then expands back into the system with a larger nonlinear front velocity so that the nonlinear structured state ultimately invades the region occupied by the homogeneous state.

The boundary in parameter space between convective and absolute instability is marked by parameter combinations for which one of the fronts of the linear wave packet reverts its propagation direction in the laboratory frame: In the convectively unstable regime this front propagates in the same direction as the center of the packet, in the absolutely unstable regime it moves opposite to it, and right on the boundary between the two regimes the front is stationary in the laboratory frame. This parameter combination can be determined by a saddle point analysis of the linear complex dispersion relation $s(k)$ over the complex k plane [46]. Here we do not display the dependence of s on the control parameters r, Re, and ψ.

The condition of vanishing front propagation velocity is equivalent to finding the parameters for which

$$\mathrm{Re}s(\kappa)=0 \tag{5.2}$$

with κ denoting the appropriate saddle position of $s(k)$ determined by solving

$$\frac{\partial s(\kappa)}{\partial \kappa}=0 \tag{5.3}$$

in the complex k plane [46]. In Appendix A 2 we describe our numerical method of finding the solution of (5.2) and (5.3). It yields the sought after surface in r-Re-ψ parameter space, e.g., in the form of a function $r_{c\text{-}a}(Re,\psi)$ depending on Re and ψ. This border $r_{c\text{-}a}$ lies above the bifurcation threshold r_c for growth of extended states. Thus for $r<r_c$ the basic conductive state is stable, for $r_c<r<r_{c\text{-}a}$ it is convectively unstable, and for $r_{c\text{-}a}<r$ it is absolutely unstable.

B. Ginzburg Landau amplitude equation approximation

To solve (5.2) and (5.3) for $r_{c\text{-}a}$ one has to determine the dispersion relation $s(k;r,Re,\psi)$ for complex k; i.e., one has to solve the eigenvalue problem (3.9) for complex k. This is in general a quite involved numerical task. A somewhat simpler, yet approximate method, is to use an expansion of $s(k;r,Re,\psi)$ that corresponds to approximate the full field equations by the Ginzburg Landau amplitude equation (GLE). We recapitulate the derivation of the relevant equations here for completeness. The comparison with results from the full field equation (Sec. V C) shows that the GLE yields quite useful approximations to the borderlines between absolute and convective instability.

1. Expansion of $s(k;r)$

Consider Re and ψ to be fixed for the moment so that we do not have to display them explicitly in the argument list of s. Under the assumptions (i) that the sought after saddle κ in the complex k plane lies close to the critical wave number k_c and (ii) that the relative distance

$$\mu_{c\text{-}a}=\frac{r_{c\text{-}a}}{r_c}-1 \tag{5.4}$$

between the convective-absolute border $r_{c\text{-}a}$ and the critical Rayleigh number r_c is small we expand

$$s(k;r)=s_c+(k-k_c)\left(\frac{\partial s}{\partial k}\right)_c+\frac{1}{2}(k-k_c)^2\left(\frac{\partial^2 s}{\partial k^2}\right)_c+\mu\left(r\frac{\partial s}{\partial r}\right)_c + (\text{higher-order terms}). \tag{5.5}$$

Here we have introduced for convenience the relative distance

$$\mu=\frac{r}{r_c}-1 \tag{5.6}$$

of the Rayleigh number r from its critical value r_c for onset of convection. The higher-order terms in (5.5) should be of order $\mu^{3/2}$ since for small $0<\mu\ll 1$ only extended perturbations with (real) wave numbers out of a band of width $k-k_c\sim\sqrt{\mu}$ can grow.

2. Relation to linear amplitude equation

The expansion coefficients of (5.5) appear also in the linear parts of the complex GLE

$$\tau_0(\partial_t+v_g\partial_x)A=[\mu(1+ic_0)+\xi_0^2(1+ic_1)\partial_x^2]A + (\text{nonlinear terms}). \tag{5.7}$$

Here $A(x,t)$ is the common complex amplitude of convection fields $\Phi=(w,\theta,c)$,

$$\Phi(x,z,t)=A(x,t)\hat{\Phi}(z)e^{i(k_c x-\omega t)}+\text{c.c.}, \tag{5.8}$$

that bifurcate out of the conductive state at $\mu=0$. The approximation (5.8) can be expected to be a good one as long as A is small and, more importantly, as long as the spatial field structure is well represented by that of the critical eigenfunctions $\hat{\Phi}(z)e^{ik_c x}$.

The relations between the expansion coefficients of s and the coefficients in the amplitude equation are

$$\left(\frac{\partial s}{\partial k}\right)_c=-i\left(\frac{\partial \omega}{\partial k}\right)_c=-iv_g, \tag{5.9a}$$

$$\left(r\frac{\partial s}{\partial r}\right)_c=r_c\left(\frac{\partial \gamma}{\partial r}-i\frac{\partial \omega}{\partial r}\right)_c=\frac{1+ic_0}{\tau_0}, \tag{5.9b}$$

$$\left(\frac{\partial^2 s}{\partial k^2}\right)_c=-\frac{2\,\xi_0^2}{\tau_0}(1+ic_1). \tag{5.9c}$$

In (5.9c) we have used the relation [40]

$$\left(\frac{\partial^2 \gamma}{\partial k^2}\right)_c=-\left(\frac{\partial \gamma}{\partial r}\frac{\partial^2 r_{\mathrm{stab}}}{\partial k^2}\right)_c \tag{5.10}$$

to relate the second k derivative of the growth rate to the critical curvature $\xi_0^2=(\partial^2 r_{\rm stab}/\partial k^2)_c/(2r_c)$ of the marginal stability curve $r_{\rm stab}(k)$. Note that the approximated dispersion relation (5.5) is precisely that of the GLE approximation.

3. Saddle and convective-absolute instability border

With the notation (5.9) the saddle κ (5.3) of the approximated dispersion (5.5) lies at

$$\kappa=k_c-\frac{(\partial s/\partial k)_c}{(\partial^2 s/\partial k^2)_c}=k_c-\frac{i}{1+ic_1}\frac{v_g\tau_0}{2\,\xi_0^2}. \tag{5.11}$$

Then the condition (5.2)

$$0=\mathrm{Re}\left[\mu\left(r\frac{\partial s}{\partial r}\right)_c-\frac{1}{2}\frac{(\partial s/\partial k)_c^2}{(\partial^2 s/\partial k^2)_c}\right] \tag{5.12}$$

yields the GLE approximation

$$\mu_{c\text{-}a}=\frac{v_g^2\tau_0^2}{4\,\xi_0^2(1+c_1^2)} \tag{5.13a}$$

or

$$r_{c\text{-}a}=(1+\mu_{c\text{-}a})r_c \tag{5.13b}$$

for the boundary between the convectively and absolutely unstable parameter regime [46–48].

C. Convective and absolute instability against S, U, and D perturbations

Here we present in Fig. 15 our numerical results for the borderlines between absolute and convective instability obtained from the full field equations (cf. Appendix A 2) in comparison with the GLE results.

There are three different types of extended perturbations in our system, namely S, U, and D, against which the basic conductive state becomes unstable at the bifurcation threshold r_c^S, r_c^U and r_c^D that have been determined in Sec. IV. Consequently one has to investigate the spatiotemporal growth behavior of three different packets consisting of superpositions of S, U, or D plane-wave perturbations. Their analysis along the lines of Sec. V A and Appendix A 2 yields three functions $r_{c\text{-}a}^S$ (circles), $r_{c\text{-}a}^U$ (upwards pointing triangles), and $r_{c\text{-}a}^D$ (downwards pointing triangles) each depending on Re and ψ that mark the boundary surfaces in r-Re-ψ parameter space between the convectively and absolutely unstable regimes of the basic state against type S, U, or D perturbations.

In order to determine the three boundaries within the GLE approximation we have determined the derivatives (5.9) of the respective eigenvalues s^S, s^U, and s^D at their respective critical points $r_c(Re,\psi)$, $k_c(Re,\psi)$ [43]. Then (5.13) yields the functions $r_{c\text{-}a}(Re,\psi)$ for the three patterns. They are shown in Fig. 15 for a few ψ as functions of Re by thick lines (S: dotted, U: full, D: dashed) together with the corresponding bifurcation thresholds r_c (thin lines). For positive Soret coupling $\psi=0.01$, 0.001 one obtains within the GLE approximation a local maximum of $r_{c\text{-}a}^S$ ($\psi=0.01$ at $Re\approx 0.25$, $\psi=0.001$ at $Re\approx 0.1$), when the product of τ_0 decreasing with Re and v_g increasing with Re reaches a maximum. In the $\psi=0.01$ case a second maximum is visible at small Re that is possibly associated with a root of c_1. In contrast $r_{c\text{-}a}^S$ of the full field equations (circles) is monotonously increasing with Re. For negative Soret coupling $\psi=-0.001$, -0.01, -0.1, and -0.25 $r_{c\text{-}a}^U$ first decreases with increasing Re, coincides at its local minimum with r_c^U when $v_g=0$, and afterwards increases with Re. The GLE approximation yields good quantitative agreement with the results of the full field equations for $r_{c\text{-}a}^U$ (upwards pointing triangles) in the vicinity of the local minimum, while for higher Re the GLE results increase more strongly. For smaller Reynolds numbers this validity range is typically enlarged down to $Re=0$ for the ψ values presented here.

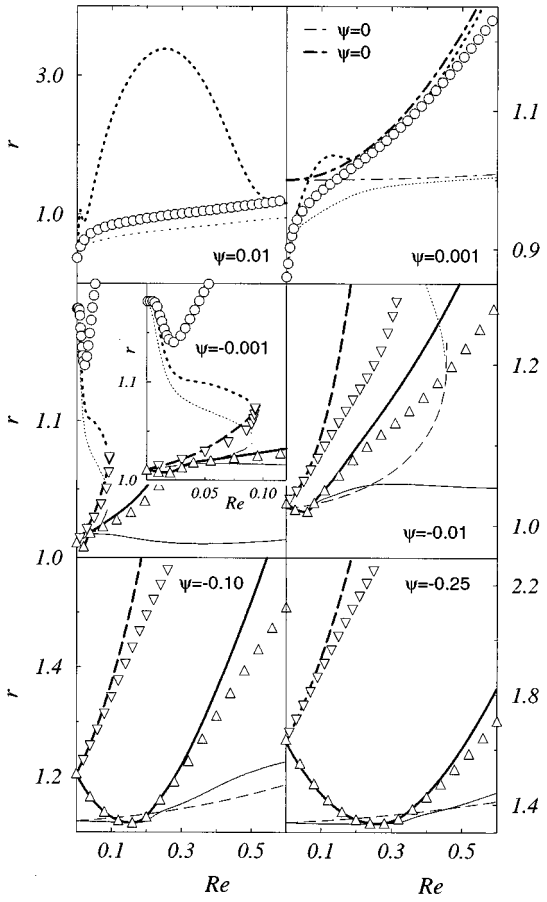

FIG. 15. Borderlines $r_{c\text{-}a}$ between absolute and convective instability versus through-flow rate. Symbols and *thick* curves represent $r_{c\text{-}a}$ obtained from the full field equations and from the GLE, respectively. *Thin* curves show stability curves r_c discussed in Sec. IV. The different types of perturbations are identified by circles and dotted lines (S), upwards pointing triangles and full lines (U), and downwards pointing triangles and dashed lines (D). The case of a pure fluid, $\psi=0$, is shown by dash-dotted lines: thick one for $r_{c\text{-}a}^S$ and thin one for r_c^S Parameters are $L=0.01, \sigma=10$, and ψ as shown.

As discussed in Sec. IV C 5 we have limited our investigation of r_c^D and r_c^S as functions of Re to cases where the wave number gap in the D-S marginal stability curves has not yet appeared. Therefore, within the GLE approximation $r_{c\text{-}a}^D$ and $r_{c\text{-}a}^S$ are determined by the expansion coefficients of s (5.9) at the critical Rayleigh number r_c only as long as the

calculation of r_c^D and r_c^S was numerically possible. Nevertheless, for higher Re critical Rayleigh numbers still exist to the left and right hand side of the wave number gap (cf. Fig. 6). We also found that the S saddle point of the full field equations (evaluated by successively increasing Re) evolves monotonously when Re increases beyond the threshold where the wave number gap occurs. The wave number of this saddle point is always above $\hat{k}=1$ and increases with Re.

The GLE results for $r_{c\text{-}a}^D$ are increasing stronger than those of the full field equations (downwards pointing triangles). For $\psi=-0.001$ the $r_{c\text{-}a}^D$ stability limit seems to terminate close to the Reynolds number where the wave number gap (cf. Sec. IV C 5) opens up in the D-S marginal stability curves. There Imκ seems to change sign when increasing Re further. A graphical analysis of this saddle that has moved into the lower complex k plane suggests that there Re$s<0$ above a certain Re limit for all r so that this saddle can be ignored.

VI. CONCLUSION

We have investigated the influence of an externally imposed horizontal shear flow on linear convective structure formation in binary fluid layers heated from below. To that end we have solved the linearized field equations for convective perturbations of the basic conductive state numerically with a shooting method. In addition we have checked our results — in particular some of the peculiar changes wih Re — by a variational calculation that gave good agreement. We have determined for positive and negative Soret coupling ψ the Re dependence of the critical bifurcation properties: stability thresholds, wave numbers, frequencies, and eigenfunctions for three different types of perturbations. The latter are identified by different characteristic exponents that cause perturbations to be stationary (S), downstream traveling (D), or upstream traveling (U) at $Re=0$.

The Hopf symmetry degeneracy of U and D perturbations at $Re=0$ and $\psi<0$ is broken by a finite through-flow — wave numbers k_c^U and k_c^D, frequencies ω_c^U and ω_c^D and bifurcation thresholds r_c^U and r_c^D develop differences. At small Re upstream traveling wave convection grows first upon increasing the heating since r_c^U is depressed and r_c^D is shifted upwards. But then, with increasing through-flow the bifurcation lines r_c^U and r_c^D intersect, giving rise to bistable bifurcation behavior. Eventually r_c^U flattens out and approaches for large Re the pure fluid's stability boundary $r_c^S(Re,\psi=0)$ — a sufficiently strong shear flow eliminates the Soret induced coupling effects between the convective concentration field and temperature and velocity fields. This also holds for mixtures with positive ψ. The bifurcation thresholds r_c^D monotonously curve upwards when increasing Re and collide with the r_c^S threshold lines that for $\psi<0$ sharply drop downwards with growing Re. This behavior is easily understood by analyzing the Re variation of the paths of the relevant three eigenvalues in the complex γ-ω plane and of the variation of $\gamma(k,r)$.

At $\psi>0$ the stationary threshold r_c^S rapidly approaches the $\psi=0$ asymptote of a pure fluid from below — again the shear flow suppresses the vertical convective transport of Soret induced concentration gradients. Thus, any Soret effect's influence on the bifurcation thresholds is eliminated by sufficiently large through-flow.

Finally we have evaluated the borders $r_{c\text{-}a}^U$, $r_{c\text{-}a}^D$, and $r_{c\text{-}a}^S$ between convective and absolute instability for U, D, and S perturbations, respectively. To that end we have determined the relevant saddles of the dispersion relations $s^U(k)$, $s^D(k)$, and $s^S(k)$ in the complex wave number plane. These numerically exact results were compared with GLE approximations, which agree reasonably well with the former. The latter were obtained by an expansion around the respective critical values and by evaluating all the coefficients that enter into the linear GLE for U, D, and S patterns.

ACKNOWLEDGMENT

Support by the Deutsche Forschungsgemeinschaft is gratefully acknowledged.

APPENDIX A: NUMERICAL ANALYSIS

1. Shooting algorithm

Here we describe our version of the shooting algorithm modified so as to better cope with the numerical problems caused by the concentration boundary layers near the horizontal plates.

The equations (3.1) are written as an eight-dimensional system of first-order differential equations

$$\partial_z \mathbf{y} - \mathcal{A}(z,\lambda)\mathbf{y}=0 \quad \text{at} \quad 0\leqslant z\leqslant 1, \tag{A1}$$

where the coefficient matrix follows directly from (3.9). The eigenvalues

$$\lambda=[r_{\text{stab}}(k),\omega(k)]_{\gamma=0} \quad \text{or} \quad \lambda=[\gamma(k),\omega(k)]_{r\,\text{fixed}} \tag{A2}$$

are determined as a function of k either for $\gamma=0$ on the marginal stability boundary $r_{\text{stab}}(k)$ or for fixed r. The eigenfunctions

$$\mathbf{y}=(w,\partial_z w,\partial_z^2 w,\partial_z^3 w,\theta,\partial_z\theta,\zeta,\partial_z\zeta) \tag{A3}$$

fulfill the boundary conditions

$$y_1=y_2=y_5=y_8=0 \quad \text{at} \quad z=0,1, \tag{A4}$$

following from (3.3).

First (A1) is integrated with a fourth-order Runge-Kutta method with the initial vectors ($z=0$)

$$\mathbf{y}^1=\hat{\mathbf{e}}_3,\ \mathbf{y}^2=\hat{\mathbf{e}}_4,\ \mathbf{y}^3=\hat{\mathbf{e}}_6,\ \mathbf{y}^4=\hat{\mathbf{e}}_7, \tag{A5}$$

where $\hat{\mathbf{e}}_j$ is the unit vector in the j direction. Then an arbitrary linear combination

$$\mathbf{y}(z)=\sum_{j=1}^{4} a_j \mathbf{y}^j(z) \tag{A6}$$

fulfills the boundary conditions at $z=0$, but not at $z=1$. The latter is guaranteed by choosing the correct coefficients a_j. This leads to a set of homogeneous equations

$$\begin{pmatrix} y_1^1 & y_1^2 & y_1^3 & y_1^4 \\ y_2^1 & y_2^2 & y_2^3 & y_2^4 \\ y_5^1 & y_5^2 & y_5^3 & y_5^4 \\ y_8^1 & y_8^2 & y_8^3 & y_8^4 \end{pmatrix}\Bigg|_{z=1} \begin{pmatrix} a_1 \\ a_2 \\ a_3 \\ a_4 \end{pmatrix} = \mathbf{0}. \tag{A7}$$

The nontrivial solution of (A7) requires the determinant of the coefficients to vanish. Thus, this solvability condition but also the explicit evaluation of the eigenvalues requires the knowledge of the eigenfunctions at $z=1$. This is a problem because of the strong variations in the boundary layers — see, e.g., Fig. 9. Our integrator is not able to shoot exactly from $z=0$ to $z=1$ so that we cannot evaluate the eigenvalues λ with a fixed accuracy. Especially, this fact makes it difficult to find a good critical wave number. To understand this, we can expand the stability curve r_{stab} around k_c^{exact},

$$\begin{aligned} \Delta r &= r_{\mathrm{stab}}(k_c^{\mathrm{exact}}+q) - r_{\mathrm{stab}}(k_c^{\mathrm{exact}}) \\ &= \frac{1}{2} q^2 \frac{\partial^2 r_{\mathrm{stab}}}{\partial k^2}\bigg|_{k_c^{\mathrm{exact}}} + O(q^3) \end{aligned} \tag{A8}$$

and we find the defect

$$q \approx \sqrt{\frac{\Delta r / r_c}{\xi_0^2}}. \tag{A9}$$

With $\xi_0^2 \sim O(1)$ the accuracy Δr strongly affects the accuracy of the critical wave number and of the coefficients entering the GLE.

One could change the integrator. But the problem can be solved more easily. Using the mirror symmetry of the eigenfunctions (w, θ, ζ) one only needs to shoot from $z=0$ to mid height $z=1/2$. There the new boundary conditions are

$$y_2 = y_4 = y_6 = y_8 = 0 \quad \text{at} \quad z = \tfrac{1}{2}. \tag{A10}$$

The new homogeneous equations replacing (A7) are then

$$\begin{pmatrix} y_2^1 & y_2^2 & y_2^3 & y_2^4 \\ y_4^1 & y_4^2 & y_4^3 & y_4^4 \\ y_6^1 & y_6^2 & y_6^3 & y_6^4 \\ y_8^1 & y_8^2 & y_8^3 & y_8^4 \end{pmatrix}\Bigg|_{z=1/2} \begin{pmatrix} a_1 \\ a_2 \\ a_3 \\ a_4 \end{pmatrix} = \mathbf{0}. \tag{A11}$$

Now, shooting only from $z=0$ to $z=1/2$ we can compute the eigenvalues with a fixed accuracy in our parameter range. A welcome secondary effect is that one saves CPU time. However, it must be said that this trick only delays the boundary layer problem without eliminating it completely: If the parameters are such that the phase velocity $|\omega_c/k_c|$ reaches about 20 the boundary layer at $z=0$ has become so thin that it is no longer possible to use our integrator.

2. Saddle point analysis

The borderline $r_{c\text{-}a}$ between convective and absolute instability is defined by the conditions (5.2) and (5.3) on the dispersion relation after a continuation into the complex wave number plane, which also gives the saddle point position κ and the frequency $\omega(\kappa)$. We have determined $\mathrm{Res}(k)$ and $\mathrm{Ims}(k)$ with a shooting method from $z=0$ to mid height $z=1/2$ (see Appendix A 1) for given r, Re, and ψ and *complex* wave number k. Then we solved for fixed Re and ψ the nonlinear system of the three equations

$$\mathrm{Res}(\kappa, r) = 0, \tag{A12}$$

$$\frac{\partial\, \mathrm{Res}(\kappa, r)}{\partial(\mathrm{Re}\kappa)} = 0, \tag{A13}$$

$$\frac{\partial\, \mathrm{Res}(\kappa, r)}{\partial(\mathrm{Im}\kappa)} = 0, \tag{A14}$$

which correspond to (5.2) and (5.3) with a Newton-Raphson method with backtracking. The solution yields the borderline value $r_{c\text{-}a}$ and the saddle position κ of s in the complex k plane.

The Jacobian matrix as well as the partial derivatives were obtained in discretized form by using central differences in the variables Rek, Imk, and r. Mainly two problems occur: one needs a good initial guess to ensure convergence of the Newton-Raphson method, and for higher Reynolds numbers, which are not discussed here, the shooting method starts to fail for the given accuracy limit (see Appendix A 1).

We also used an alternative iterative method to evaluate the saddle points. It yields the same results as our first method, but it does not require partial derivatives. First we calculate the eigenvalue

$$[\omega(\tilde{\kappa}), r(\tilde{\kappa})]_{\gamma=0} \tag{A15}$$

at a suitably chosen initial value $\tilde{\kappa}$ for the saddle position. Then, along a circle in the complex k plane of radius ρ around $\tilde{\kappa}$ we determine, say, $n \simeq 10$ values

$$[\omega(k_j), \gamma(k_j)]_{r=r(\tilde{\kappa})}, \quad j = 0, \ldots, n-1 \tag{A16}$$

with

$$k_j = \tilde{\kappa} + \rho\left[\cos\left(\frac{2j\pi}{n}\right) + i \sin\left(\frac{2j\pi}{n}\right)\right]. \tag{A17}$$

The function values $\{\omega(\tilde{\kappa}), \omega(k_0), \ldots, \omega(k_{n-1})\}$ are then used for a biquadratical fit

$$\begin{aligned} \omega(k) = a_0 &+ a_1 \mathrm{Im}k + a_2 \mathrm{Re}k + a_3 (\mathrm{Im}k)^2 + a_4 (\mathrm{Re}k)^2 \\ &+ a_5 \mathrm{Im}k\ \mathrm{Re}k \end{aligned} \tag{A18}$$

and the analytically determined saddle of (A18) is used as a new initial value $\tilde{\kappa}$. Now, we reduce the circle radius ρ by a factor α and continue as above. We repeat this procedure until the changes of $\tilde{\kappa}$ have fallen below a suitable limit. This method is fast, robust, and easily programmable. However, the first ρ and the reducing factor α have to be chosen carefully. Typically we put $\rho \sim O(10^{-2})$ and $\alpha = \sqrt{2}$.

APPENDIX B: COMPARISON WITH A VARIATIONAL METHOD

In view of the unexpected Re dependence, say, of Fig. 2 we wanted to compare our results obtained with a shooting method with a completely different and independent method.

To that end we used the variational method of Prigogine and Glandsdorff [49,50]. While this method does not yield exact results it still is very valuable in providing an independent check for our numerical analysis.

The aim of this variational method is to find a functional, called the local potential, and to minimize it. We start with the linearized field equations

$$\partial_t u = -\sigma\ Re\ P\partial_x u - \partial_x p + \sigma\nabla^2 u - \sigma\ Re\ w\partial_z P, \tag{B1a}$$

$$\partial_t w = -\sigma\ Re\ P\partial_x w - \partial_z p + \sigma\nabla^2 w + \sigma[(1+\psi)\theta + \zeta], \tag{B1b}$$

$$\partial_t \theta = -\sigma\ Re\ P\partial_x \theta + \nabla^2\theta + Ra\, w, \tag{B1c}$$

$$\partial_t \zeta = -\sigma\ Re\ P\partial_x \zeta + L\nabla^2\zeta - \psi\nabla^2\theta, \tag{B1d}$$

$$0 = \partial_x u + \partial_z w. \tag{B1e}$$

Here u, w, θ, ζ, and p are convective disturbances from the conductive profiles and $P(z)$ the Poiseuille shear flow (2.8b). Following the procedure explained in Ref. [49] we multiply the above equations by increments of the respective fields: (B1a) by $-\delta u$, (B1b) by $-\delta w$, (B1c) by $-\delta\theta$, and (B1d) by $-\delta\zeta$. Here, e.g.,

$$w = w^0 + \delta w \tag{B2}$$

with w^0 being a solution of (B1) that is not varied in the following. Then we add and obtain

$$\begin{aligned}
&-\tfrac{1}{2}\partial_t[(\delta u)^2+(\delta w)^2+(\delta\theta)^2+(\delta\zeta)^2] \\
&\quad = \partial_t u^0\,\delta u + \partial_t w^0\,\delta w + \partial_t\theta^0\,\delta\theta + \partial_t\zeta^0\,\delta\zeta \\
&\qquad + \sigma\ Re\ P\partial_x u\,\delta u + \sigma\ Re\ w\partial_z P\,\delta u \\
&\qquad + \partial_x p\,\delta u - \sigma\,\delta u\nabla^2 u + \sigma\ Re\ P\partial_x w\,\delta w \\
&\qquad - \sigma\,\delta w[(1+\psi)\theta+\zeta] - \sigma\,\delta w\nabla^2 w - Ra\ w\,\delta\theta \\
&\qquad - \delta\theta\nabla^2\theta + \sigma\ Re\ P\partial_x\theta\,\delta\theta + \partial_z p\,\delta w \\
&\qquad - L\,\delta\zeta\nabla^2\zeta + \psi\,\delta\zeta\nabla^2\theta + \sigma\ Re\ P\partial_x\zeta\,\delta\zeta
\end{aligned} \tag{B3}$$

when making use of relations such as

$$-\partial_t w\,\delta w = -\partial_t(w^0+\delta w)\,\delta w = -\tfrac{1}{2}\partial_t(\delta w)^2 - \partial_t w^0\,\delta w. \tag{B4}$$

We expand the fields in plane waves, $\Phi = \hat{\Phi}(z)e^{ikx}e^{st}$, and we integrate over the entire x-z cross section of the fluid layer. Following closely the prescriptions of Ref. [50] we then obtain the local potential

$$\begin{aligned}
\Psi = \int_0^1 dz\Bigg[& \frac{s}{k^2}\partial_z\hat{w}^0\partial_z\hat{w} + s(\hat{w}^0\hat{w} + \hat{\theta}^0\hat{\theta} + \hat{\zeta}^0\hat{\zeta}) \\
& + \sigma\partial_z\hat{w}^0\partial_z\hat{w} - \frac{\sigma}{2\,k^2}(\partial_z^2\hat{w})^2 + \frac{2\,\sigma}{k^2}\partial_z^2\hat{w}^0\partial_z^2\hat{w} \\
& + ik\sigma\ Re\ P(\hat{w}^0\hat{w} + \hat{\theta}^0\hat{\theta} + \hat{\zeta}^0\hat{\zeta}) + \frac{\sigma}{2}(\partial_z\hat{w})^2 \\
& + \sigma k^2\left(\hat{w}^0\hat{w} + \frac{1}{\sigma}\hat{\theta}^0\hat{\theta} + \frac{L}{\sigma}\hat{\zeta}^0\hat{\zeta}\right) - \sigma(1+\psi)\hat{\theta}^0\hat{w} \\
& - Ra\ \hat{w}^0\hat{\theta} + \frac{1}{2}(\partial_z\hat{\theta})^2 + \frac{L}{2}(\partial_z\hat{\zeta})^2 - \sigma\hat{\zeta}^0\hat{w} - \psi k^2\hat{\theta}^0\hat{\zeta} \\
& + \psi\partial_z^2\hat{\theta}^0\hat{\zeta} - \frac{i}{k}\sigma\ Re\ \hat{w}^0\partial_z\hat{w}\partial_z P + \frac{i}{k}\sigma\ Re\ P\partial_z\hat{w}^0\partial_z\hat{w}\Bigg].
\end{aligned} \tag{B5}$$

Here we have elimitated the pressure by using (B1a):

$$\begin{aligned}
-\hat{p}^0 = & \frac{s}{k^2}\partial_z\hat{w}^0 + \frac{i}{k}\sigma\ Re\ P\partial_z\hat{w}^0 - \frac{i}{k}\sigma\ Re\ \hat{w}^0\partial_z P - \frac{\sigma}{k^2}\partial_z^3\hat{w}^0 \\
& + \sigma\partial_z\hat{w}^0.
\end{aligned} \tag{B6}$$

Furthermore, partial integrations in z have been applied. One can check directly that the Euler-Langrange equation for, say, $\hat{\zeta}$,

$$\frac{\partial\Psi}{\partial\hat{\zeta}} - \frac{\partial}{\partial z}\frac{\partial\Psi}{\partial(\partial\hat{\zeta}/\partial z)} = 0, \tag{B7}$$

leads to

$$[s + ik\sigma\ Re\ P]\hat{\zeta}^0 = L(\partial_z^2\hat{\zeta} - k^2\hat{\zeta}^0) - \psi(\partial_z^2 - k^2)\hat{\theta}^0. \tag{B8}$$

This is together with the *a posteriori* subsidiary condition $\hat{\zeta} = \hat{\zeta}^0$ the Eq. (B1d). An analogous calculation leads with respective subsidiary conditions $\hat{\theta} = \hat{\theta}^0$, $\hat{w} = \hat{w}^0$ to the other differential equations.

To get the critical values we expand the unknows $\hat{w}, \hat{\theta}$, and $\hat{\zeta}$,

$$\hat{w}(z) = \sum_{j=1}^{N_1} \tilde{w}_j f_j(z), \quad \hat{w}^0(z) = \sum_{j=1}^{N_1} \tilde{w}_j^0 f_j(z), \tag{B9a}$$

$$\hat{\theta}(z) = \sum_{j=1}^{N_2} \tilde{\theta}_j g_j(z), \quad \hat{\theta}^0(z) = \sum_{j=1}^{N_2} \tilde{\theta}_j^0 g_j(z), \tag{B9b}$$

$$\hat{\zeta}(z) = \sum_{j=1}^{N_3} \tilde{\zeta}_j h_j(z), \quad \hat{\zeta}^0(z) = \sum_{j=1}^{N_3} \tilde{\zeta}_j^0 h_j(z) \tag{B9c}$$

in functions f_j, g_j, and h_j that satisfy the NSI boundary conditions. As trial functions we use

$$f_j(z) = [z(1-z)]^{2j}, \tag{B10a}$$

$$g_j(z) = z(1-z)(2z-1)^{2(j-1)}, \tag{B10b}$$

$$h_j(z)=[z(1-z)]^{2(j-1)}. \tag{B10c}$$

We insert (B9) and (B10) into the expression for Ψ, we minimize with respect to the variational parameters $\tilde{w}_j$, $\tilde{\theta}_j$, and $\tilde{\zeta}_j$, and we use the subsidiary conditions

$$\tilde{w}_j=\tilde{w}_j^0, \quad \tilde{\theta}_j=\tilde{\theta}_j^0, \quad \tilde{\zeta}_j=\tilde{\zeta}_j^0. \tag{B11}$$

Then we obtain a system of $N=N_1+N_2+N_3$ linear homogeneous equations $\mathcal{A}\mathbf{x}=\mathbf{0}$ where the vector $\mathbf{x}$ has N components containing $\tilde{w}_j^0$, $\tilde{\theta}_j^0$, and $\tilde{\zeta}_j^0$. For nontrivial solutions to exist the determinant of $\mathcal{A}$ must be zero, so that we have to solve the equation

$$\det\mathcal{A}[r_{\mathrm{stab}}(k),\omega(k)]_{\gamma=0}=0. \tag{B12}$$

With $N_1=1$, $N_2=3$, $N_3=4$ the software package MATHEMATICA is able to solve (B12) exactly.

The variational results display the same structural properties as the shooting results and they agree within less than 1%–2% for $Re\neq 0$. For $Re=0$ the agreement is better. We found, e.g., for $\psi=-0.25$ the critical values $r_c=1.33497$, $\hat{k}_c=1.00451$, and $\omega_c=\pm 11.20027$ differing by less than 0.2% from the shooting results. As an interesting aside we mention that the variational calculus yields in the absence of through-flow $\psi_\infty^0=-L/(1+L)$ exactly. Furthermore, the separation ratio ψ_0 for which $k_c=0$ is obtained as $\psi_0=L/(f-L)$ with $f=6695603/25739142=0.2601\ldots$, which has to be compared with the analytically exact result $f=34/131=0.2595\ldots$ [41,37].

[1] M. C. Cross and P. C. Hohenberg, Rev. Mod. Phys. **65**, 851 (1993).

[2] M. A. Dominguez-Lerma, G. Ahlers, and D. S. Cannell, Phys. Rev. E **52**, 6159 (1995); K. Lerman, E. Bodenschatz, D. S. Cannell, and G. Ahlers, Phys. Rev. Lett. **70**, 3572 (1993).

[3] E. Kaplan, E. Kusnetsov, and V. Steinberg, Phys. Rev. E **50**, 3712 (1994).

[4] P. Kolodner, Phys. Rev. E **47**, 1038 (1993).

[5] A. La Porta, K. D. Eaton, and C. M. Surko, Phys. Rev. E **53**, 570 (1996).

[6] P. Le Gal, A. Pocheau, and V. Croquette, Phys. Rev. Lett. **54**, 2501 (1985); V. Croquette, Contemp. Phys. **30**, 113 (1989); **30**, 153 (1989).

[7] O. Lhost and J. K. Platten, Phys. Rev. A **40**, 6415 (1989).

[8] M. Liu and J. R. de Bruyn, Can. J. Phys. **70**, 689 (1992).

[9] E. Moses and V. Steinberg, Phys. Rev. A **43**, 707 (1991); V. Steinberg and E. Kaplan, in *Spontaneous Formation of Space-Time Structures and Criticality*, edited by T. Riste and D. Sherrington (Kluwer Academic Publishers, Boston, 1991), p. 207.

[10] G. Zimmermann, U. Müller, and S. H. Davis, J. Fluid Mech. **238**, 657 (1992); **254**, 720 (1993).

[11] D. Bensimon, A. Pumir, and B. I. Shraiman, J. Phys. (Paris) **50**, 3089 (1989).

[12] H. R. Brand, P. S. Lomdahl, and A. C. Newell, Physica D **23**, 345 (1986).

[13] T. Clune and E. Knobloch, Phys. Rev. A **44**, 8084 (1991).

[14] M. C. Cross, Phys. Rev. A **38**, 3593 (1988).

[15] St. Hollinger, P. Büchel, and M. Lücke (unpublished).

[16] S. J. Linz, M. Lücke, H. W. Müller, and J. Niederländer, Phys. Rev. A **38**, 5727 (1988).

[17] H. W. Müller and M. Lücke, Phys. Rev. A **38**, 2965 (1988).

[18] W. Barten, M. Lücke, M. Kamps, and R. Schmitz, Phys. Rev. E **51**, 5636 (1995); **51**, 5662 (1995).

[19] M. Bestehorn, Physica D **61**, 59 (1992); Phys. Lett. A **174**, 43 (1993).

[20] A. E. Deane, E. Knobloch, and J. Toomre, Phys. Rev. A **36**, 2862 (1987).

[21] H. Yahata, Prog. Theor. Phys. Suppl. **99**, 493 (1989); Prog. Theor. Phys. **85**, 933 (1991).

[22] See Refs. [23,24] for early overviews and Refs. [1,18] for further references also on spatially localized convection structures.

[23] J. K. Platten and J. C. Legros, *Convection in Fluids* (Springer Verlag, Berlin, 1984).

[24] R. P. Behringer, Rev. Mod. Phys. **57**, 657 (1985).

[25] D. P. Chock and C.-H. Li, Phys. Fluids **18**, 1401 (1975).

[26] D. Gutkowicz-Krusin, M. A. Collins, and J. Ross, Phys. Fluids **22**, 1443 (1979); **22**, 1451 (1979).

[27] G. W. T. Lee, P. Lucas, and A. Tyler, J. Fluid Mech. **135**, 235 (1983).

[28] H. Gao and R. P. Behringer, Phys. Rev. A **34**, 697 (1986).

[29] P. Kolodner, A. Passner, C. M. Surko, and R. W. Walden, Phys. Rev. Lett. **56**, 2621 (1986).

[30] W. Hort, Diplomarbeit, Universität Saarbrücken, 1988.

[31] E. Knobloch and D. R. Moore, Phys. Rev. A **36**, 860 (1988).

[32] M. C. Cross and K. Kim, Phys. Rev. A **37**, 3909 (1988); **38**, 529 (1988).

[33] W. Schöpf and W. Zimmermann, Europhys. Lett. **8**, 41 (1989); Phys. Rev. E **47**, 1739 (1993).

[34] N. D. Stein, Phys. Rev. A **43**, 768 (1991).

[35] O. Lhost, S. J. Linz, and H. W. Müller, J. Phys. (France) II **1**, 279 (1991).

[36] W. Hort, S. J. Linz, and M. Lücke, Phys. Rev. A **45**, 3737 (1992).

[37] St. Hollinger and M. Lücke, Phys. Rev. E **52**, 642 (1995).

[38] H. B. Squire, Proc. R. Soc. London A **142**, 621 (1933).

[39] S. Chandrasekhar, *Hydrodynamic and Hydromagnetic Stability* (Oxford University Press, New York, 1981).

[40] A. C. Newell, Lect. Appl. Math. **15**, 157 (1974).

[41] E. Knobloch, Phys. Rev. A **40**, 1549 (1989).

[42] H. W. Müller, M. Lücke, and M. Kamps, Europhys. Lett. **10**, 451 (1989); Phys. Rev. A **45**, 3714 (1992).

[43] Ch. Jung, Diplomarbeit, Universität Saarbrücken, 1993.

[44] A. Bers, *Linear Waves and Instabilities* (Physique des Plasmas, New York, 1975).

[45] R. J. Briggs, *Electron-Stream Interaction with Plasmas*, Research Monograph No. 29 (MIT Press, Cambridge, MA, 1964).

[46] P. Huerre, in *Instabilities and Nonequilibrium Structures*, ed-

ited by E. Tirapegui and D. Villaroel (Reidel, Dordrecht, Holland, 1987), p. 141.

[47] P. Huerre, in *Propagation in Systems far from Equilibrium*, edited by J. E. Wesfreid, H. R. Brand, P. Manneville, G. Albinet, and N. Boccara (Springer-Verlag, Berlin, 1988), p. 340.

[48] R. J. Deissler, J. Stat. Phys. **40**, 371 (1985).

[49] P. Glandsdorff and I. Progogine, Physica **30**, 351 (1964); I. Progogine and P. Glandsdorff, *ibid.* **31**, 1242 (1965); *Thermodynamic and Theory of Structure, Stability and Fluctuations* (Wiley-Interscience, London, 1971).

[50] J. K. Platten, Int. J. Eng. Sci. **9**, 37 (1971); **9**, 855 (1971).